POLITECNICO DI TORINO

MASTER's Degree in COMMUNICATIONS ENGINEERING

Politecnico di Torino

MASTER's Degree Thesis

GNSS to Lunar navigation systems: Fused approaches and handover based on a lunar beacon

Supervisors

Prof. Fabio DOVIS
Dr. Alex MINETTO
Dr. Andrea NARDIN

Candidate

VLAD SILEA

Academic Year 2024/2025

Abstract

The renewed international interest in lunar exploration has made the establishment of reliable Positioning, Navigation and Timing (PNT) services beyond Earth orbit a strategic priority. As upcoming missions extend further into cislunar space and onto the lunar surface, autonomous navigation becomes essential to ensure operational continuity without constant reliance on ground-based tracking networks. Global Navigation Satellite Systems (GNSS), although originally designed for terrestrial and near-Earth users, have already demonstrated their usefulness for a variety of space applications. The Lunar GNSS Receiver Experiment (LuGRE), developed under an agreement between the Italian Space Agency (ASI) and NASA, has confirmed the feasibility of receiving and processing GPS and Galileo signals in cislunar space and on the lunar surface, demonstrating the potential of GNSS to support navigation well beyond Earth orbit. However, at these distances, signals are extremely weak and all visible satellites appear clustered within a narrow angular region around Earth, leading to unfavorable geometry and degraded positioning accuracy. This thesis provides a quantitative assessment of GNSS performance in the cislunar environment and investigates how it can be enhanced through the inclusion of a lunar surface beacon transmitting GNSS-like signals. A dedicated MATLAB-based simulation framework was developed and extensively improved for this purpose. The simulator was upgraded to support all major global and regional constellations (GPS, Galileo, GLONASS, BeiDou, QZSS and IRNSS), realistic multi-frequency antenna radiation patterns, and detailed link-budget modelling. A configurable lunar beacon model was integrated, allowing the evaluation of different transmitter powers, antenna patterns and three pointing strategies: mutual pointing, dual Earth-pointing and a hybrid configuration combining the two approaches. The simulator predictions of satellite visibility were validated using real GNSS data collected with a high-end Septentrio receiver connected to the reference antenna located on the roof of the DET building at Politecnico di Torino. Simulation results in the cislunar environment show that, while GNSS constellations ensure nearly continuous signal availability along an Earth–Moon transfer orbit, the satellite geometry remains weak, leading to Geometric Dilution of Precision (GDOP) values typically ranging between 50 and 300, with peaks exceeding 600 during the worst

geometric conditions. In this regard, the inclusion of a single beacon on the lunar surface markedly improves the overall geometry. In particular, with the hybrid pointing configuration, GDOP values are reduced by more than an order of magnitude, resulting in a positioning error standard deviation between 50 and 150 metres for most of the trajectory, compared to several kilometres in the GNSS-only case. These findings highlight the effectiveness of surface beacons as lightweight and cost-efficient augmentation elements for future lunar navigation systems, contributing to the design of reliable and autonomous PNT architectures for the upcoming era of deep-space exploration.

Table of Contents

List of Tables

List of Figures

Acronyms

ASI Agenzia Spaziale Italiana

CDF Cumulative Distribution Function

CLPS Commercial Lunar Payload Services

C/N_0 carrier-to-noise density ratio

DOP Dilution of Precision

DSN Deep Space Network

DTN Delay/Disruption Tolerant Networking

ECEF Earth-Centered, Earth-Fixed

EIRP Effective Isotropic Radiated Power

EKF Extended Kalman Filter

ESA European Space Agency

FOC Full Operational Capability

GCF gain correction factor

GDOP Geometric Dilution of Precision

GEO Geostationary Orbit

GNSS Global Navigation Satellite Systems

GNSS-R GNSS Reflectometry

GPS Global Positioning System

GRAP Galileo Reference Antenna Pattern

HEO Highly Elliptical Orbit

IGS International GNSS Service

IRNSS Indian Regional Navigation Satellite System

JAXA Japan Aerospace Exploration Agency

JPL Jet Propulsion Laboratory

JRC Joint Research Centre

LCNS Lunar Communications and Navigation Services

LEO Low Earth Orbit

LNIS LunaNet Interoperability Specification

LMS Least-Mean-Squares

LO Lunar Orbit

LOS Line of Sight

LuGRE Lunar GNSS Receiver Experiment

NAV Navigation message

NASA National Aeronautics and Space Administration

POD Precise Orbit Determination

PNT Positioning, Navigation and Timing

PRN Pseudo-Random Noise (spreading code)

PVT Position, Velocity, Time

QZSS Quasi-Zenith Satellite System

RINEX Receiver Independent Exchange Format

RTN Real-Time Navigation

SCaN Space Communications and Navigation

SPP Single Point Positioning

SSV Space Service Volume

SSTL Surrey Satellite Technology Ltd.

TA-EKF Trajectory-Aware Extended Kalman Filter

TEC Total Electron Content

TLO Translunar Orbit

UERE User Equivalent Range Error

UNOOSA United Nations Office for Outer Space Affairs

UTC Coordinated Universal Time

WGS84 World Geodetic System 1984

Chapter 1

Introduction

Lunar exploration is increasingly highlighting the need for reliable Positioning, Navigation and Timing (PNT) services in cislunar space. Current space operations still rely heavily on ground-segment assets: radio-frequency tracking through Deep Space Network (DSN) facilities and direct-to-Earth links enables accurate orbit determination, but it also implies elevated operational costs and a strong dependence on limited ground resources [1]. As the number of lunar and deep-space missions grows, this model becomes difficult to sustain and enhancing on-board autonomy is becoming a key objective of future exploration roadmaps [2]. Traditional Earth-based tracking requires continuous visibility from the ground and inevitably constrains when and how spacecraft can operate. This is one of the reasons why extracting navigation information directly from signals available in space is becoming increasingly relevant.

The growing number of lunar initiatives has drawn attention to these limitations. Programs such as National Aeronautics and Space Administration (NASA)'s Artemis [3] and European Space Agency (ESA)'s Moonlight initiative [4] highlight the importance of developing new infrastructures to support cislunar operations (Fig. 1.1). Reliable navigation is essential not only for human missions and surface activities, but also for robotic exploration, logistics and scientific payloads. Recent studies have outlined how dedicated lunar communication and navigation infrastructures, possibly supported by Global Navigation Satellite Systems (GNSS)-based services, could address these needs in a scalable way [5].

In this context, GNSS represents a valuable opportunity. Although conceived for users on Earth, it has already been exploited successfully in high-altitude missions and is now being considered as a complementary resource for lunar navigation. More recently, the Lunar GNSS Receiver Experiment (LuGRE) [6], developed in collaboration between NASA and the Italian Space Agency, has collected data in cislunar space and on the lunar surface, demonstrating that GNSS signals can indeed be acquired and processed even at lunar distances. These results confirm

the potential of GNSS to support navigation well beyond Earth orbit, while also highlighting the need for complementary solutions when signal availability and geometry become limiting factors.

It is clear that GNSS alone cannot meet the requirements of future lunar operations. The combination of weak signals and unfavourable geometry makes it necessary to consider augmentation strategies. One of the most promising options is the use of lunar surface beacons transmitting in GNSS frequency bands, which could improve availability, strengthen geometry and support seamless transitions between different navigation sources. Although this thesis focuses on the Earth–Moon system, the idea behind these beacons is not limited to the lunar case. Similar solutions could play a role in other deep-space environments, where spacecraft face comparable limitations in terms of radiometric geometry and received signal power. In that sense, beacons deployed other planets can be seen as a natural extension of this concept, offering additional reference signals to support autonomous navigation during interplanetary transfers.

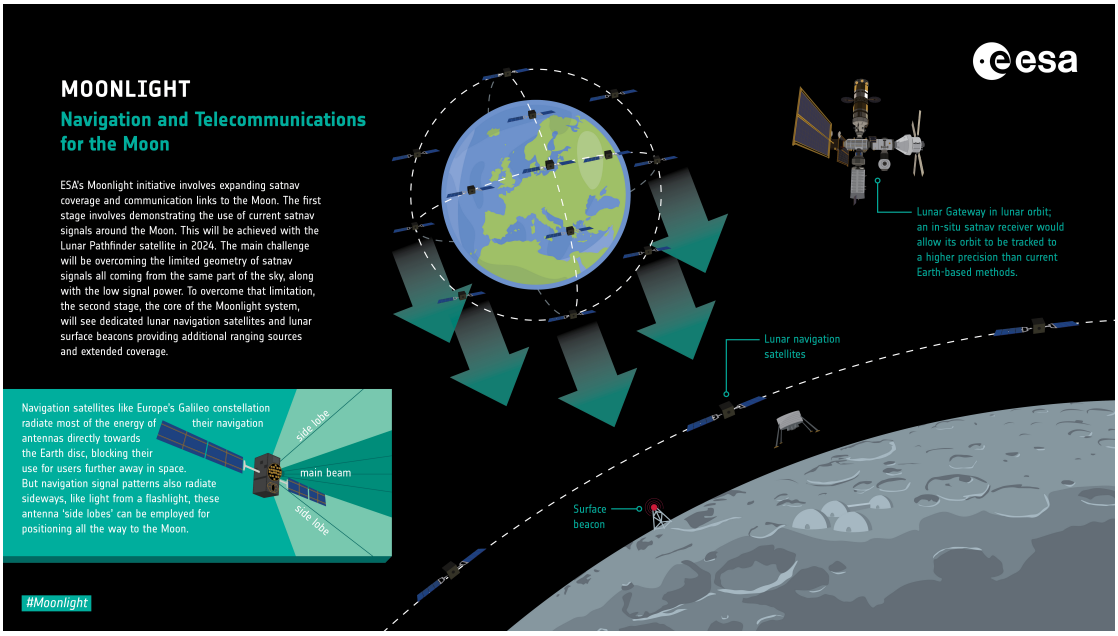

Figure 1.1: ESA Moonlight initiative concept: extension of GNSS coverage to the Moon through lunar navigation satellites and surface beacons. *Credit: ESA*

1.1 GNSS for Space Applications

GNSS systems were originally designed to provide PNT services to terrestrial users. Over the last four decades, however, their role has expanded well beyond

the Earth's surface and the use of GNSS in space has become essential in many cases. The first demonstration dates back to 1982, when the GPSPAC receiver on board Landsat-4 successfully acquired GPS signals in Low Earth Orbit (LEO), proving the feasibility of GNSS for space applications [7]. Since then, continuous developments in receiver technology and antenna design have transformed GNSS from an experimental capability to a standard component of space missions.

One of the most important applications of GNSS in space is autonomous orbit determination. In LEO, GNSS has become the default technique for Precise Orbit Determination (POD), delivering meter-level accuracy in real time [8]. This allows satellites to operate with reduced reliance on ground tracking networks and has proven particularly valuable for Earth observation, telecommunications and small satellite missions.

At higher orbital regimes, such as Geostationary Orbit (GEO), signal reception becomes more challenging because satellites at approximately 36 000 km altitude are above the GNSS constellation orbiting at 20 000 km altitude. In these cases, both the main-lobe and the side-lobe emissions of GNSS satellite antennas can be received, depending on the position of the spacecraft and the orientation of the transmit antenna. A schematic representation of this geometry is shown in Fig. 1.2.

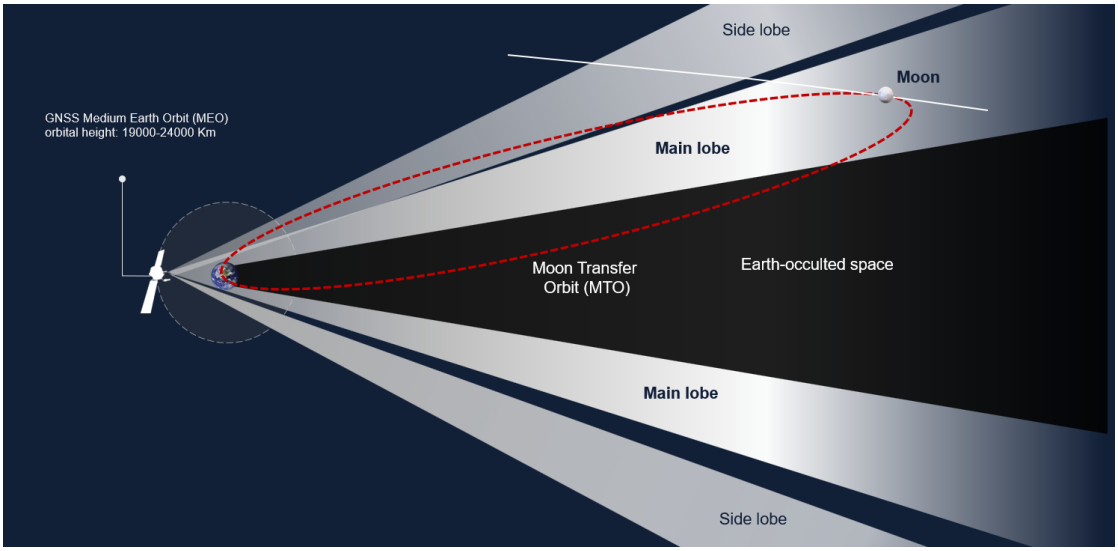

Figure 1.2: Geometric visibility of GNSS main-lobe and side-lobe emissions as seen from high-altitude spacecraft.

Despite this limitation, several missions have demonstrated that these signals can still provide useful performance for orbit determination at high altitudes [9].

GNSS also enables Real-Time Navigation (RTN), where orbit propagators running on board are continuously updated with GNSS measurements [2]. This

approach enhances spacecraft autonomy and improves orbital knowledge to the decameter level when multi-constellation, multi-frequency receivers are employed. Moreover, GNSS has been successfully used to support advanced maneuvers such as rendezvous and docking, formation flying and GEO station keeping [10].

Beyond orbit determination, GNSS plays a central role in providing precise timing in space. Synchronization to GNSS system time ensures direct and accurate access to Coordinated Universal Time (UTC), which is essential for time-stamping scientific data, coordinating multiple instruments and enabling inter-satellite synchronization. Relying on GNSS for timing significantly reduces the dependence on very stable and costly on-board clocks. For missions involving satellite constellations or distributed sensors, GNSS-based time transfer ensures that all units share a common reference, enabling coherent operations. This capability has become increasingly relevant in the context of cooperative satellite systems and networks, where a reliable timing standard supports both communications and navigation services.

GNSS can also contribute to attitude determination. Although not as accurate as dedicated sensors, GNSS can be adopted as a primary attitude source in missions with moderate accuracy requirements or more typically as a complementary or backup solution, reinforcing the performance and robustness of more accurate systems such as star trackers, contributing to the reliability of the overall navigation system [11].

In some missions, GNSS receivers are included not only as navigation sensors but also as scientific payloads. Measurement of signal characteristics enable radio-occultation studies, altimetry analysis and the estimation of ionospheric parameters such as the Total Electron Content (TEC) [12].

Another important application is GNSS Reflectometry (GNSS-R), where the reflections of GNSS signals from the Earth's surface are analyzed. This technique has found applications in monitoring wind and waves, soil moisture, water detection, vegetation classification and many others, expanding the role of GNSS from being purely a navigation infrastructure to becoming a valuable source of scientific information [13].

Although GNSS has proven indispensable in Earth's orbits, its potential use extends to more distant scenarios. During Translunar Orbit (TLO) and Lunar Orbit (LO), GNSS signals can be exploited to provide orbital monitoring, trajectory support and to deliver backup navigation information, reducing tracking and operations costs [10].

Future lunar applications may also include Moon Surface Positioning, where GNSS signals could provide partial coverage until dedicated lunar constellations become available. Demonstrations such as LuGRE, which was previously mentioned, aim to characterize signal reception at lunar distances and to assess the feasibility of standalone navigation on the Moon. These initiatives underline the growing interest in extending GNSS capabilities into the cislunar domain, where they could

complement emerging lunar navigation infrastructures.

All these developments demonstrate that GNSS, while conceived for terrestrial users, has progressively expanded its role to include a wide variety of space applications and is now being investigated as a potential contributor to future lunar and cislunar missions.

1.2 Challenges of GNSS in Cislunar Space

The extension of GNSS to the cislunar domain faces several limitations that derive from the fundamental design of the constellations. These systems were conceived to serve terrestrial and near-Earth users, therefore several aspects of their signal structure and geometry become critical when the user is placed at lunar distances.

A first difficulty lies in the visibility of the constellation. From the Moon GNSSs satellites appear concentrated in a narrow region around the Earth and the number of signals available at the same time is drastically reduced compared to terrestrial conditions. This configuration produces unfavorable Dilution of Precision (DOP) values, as the line of sight lacks angular diversity. The situation may become even worse then Earth occultation occurs, which may hide part of the constellation from the point of view, as showed in Fig. 1.2. The geometry alone imposes a fundamental constraint on the achievable positioning accuracy [14].

The second issue is the received signal power. Free-space path loss at distances on the order of 384 000 km results in a dramatic reduction of the carrier-to-noise density ratio (C/N_0). In most cases lunar receivers are also limited to exploiting the side-lobes of GNSS transmitting antennas, since the main beams are directed toward Earth. Side-lobe reception not only decreases the average received power but also introduces strong variability depending on the satellite orientation and the receiving antenna pointing. The use of high-gain receiver antennas on board can partly mitigate these effects, improving the link margin and increasing the probability of tracking multiple sources. Nevertheless, high sensitivity in acquisition and tracking remains essential to operate in such low signal conditions.

Additional limitations emerge from acquisition process itself [15]. At lunar distances, the receiver must detect and track signals with extremely low power, which implies that the probability of false alarm in the acquisition process becomes a central concern. The decision threshold is chosen to keep the system false alarm probability P_{FA} within acceptable limits. Considering N_{SS} independent cells in the time-frequency search space, the probability that at least one of them crosses the threshold in absence of signal is given by

$$P_{FA} = 1 - (1 - p_{fa})^{N_{SS}} \tag{1.1}$$

where p_{fa} is the cell false alarm probability. It is evident that as the number of

bins N_{SS} increases, the overall P_{FA} rapidly grows, even if the individual p_{fa} remains small. This behaviour forces the receiver either to accept a higher probability of false detection or to increase the threshold β, with the consequence of reducing sensitivity and making weak signals harder to detect. In this context, accurate external aiding is extremely valuable, especially in the Doppler domain, because it reduces the size of the search space and thus the number of bins to be tested.

The Doppler effect on spreading codes also represents a critical source of difficulty. The Doppler frequency impacts the effective chipping rate of the received Pseudo-Random Noise (spreading code) (PRN) sequence, which can be expressed as

$$R_c = R_{c,\text{nom}} \left(1 + \frac{f_D}{f_L}\right) \tag{1.2}$$

where:

- R_c is the effective chipping rate of the received code,
- $R_{c,\text{nom}}$ is the nominal chipping rate of the PRN sequence,
- f_D is the Doppler frequency shift observed at the receiver,
- f_L is the carrier frequency of the transmitted signal.

This relation shows that the received code may appear stretched or compressed with respect to the local replica and after a certain interval it slips by one chip, producing a loss of alignment. The consequence is that the maximum coherent integration time achievable before the chip slip effect is limited by the presence of the Doppler shift. This situation is particularly challenging because longer integration times are normally required to improve acquisition sensitivity, while at the same time the Doppler shift restricts the usable interval before the chip slip effect occurs. In order to overcome this contradiction, compensation techniques are necessary. Carrier Doppler can be addressed through de-chirping, which removes the frequency variation across the correlation window and sharpens the correlation peak in the Doppler domain. The impact on the code can instead be mitigated by generating local replicas with a chipping rate matched to the actual received sequence [15].

Overall, the combination of poor geometry, weak and variable signal power, high sensitivity requirements and Doppler-induced distortions defines an environment well beyond the design assumptions of GNSS constellations. Extending GNSS-based navigation to the cislunar domain therefore demands specialized receiver architectures and external augmentation support to ensure reliable performance.

1.3 Purpose and Structure of the Thesis

Having outlined the context and the main challenges related to the use of GNSS beyond Earth orbit, this section defines the objectives of the work and describes the organization of the thesis.

The purpose of this study is to evaluate the feasibility of GNSS-based navigation in the cislunar environment and to explore possible approaches to extend its effective coverage. The analysis focuses on quantifying the limitations imposed by weak signals and poor geometry at lunar distance, and on assessing how additional elements, such as a lunar surface beacon, could improve positioning performance. The overall goal is to characterize the radiometric and geometric conditions affecting GNSS performance at lunar distances, through the analysis of parameters such as signal power, C/N_0, satellite visibility and DOP, both for standalone GNSS and for configurations including a lunar beacon.

The work has been carried out using a pre-existing simulation framework that was specifically extended for this research. In particular, the following contributions were developed as part of this thesis:

- inclusion of support for multiple GNSSs constellations within the simulation environment;
- integration of realistic transmit and receive antenna radiation patterns, enabling a more accurate link budget and visibility analysis;
- design and modelling of a lunar surface beacon transmitting in GNSS frequency bands;
- experimental validation of the simulator using real GNSS data collected with a high-end receiver, allowing a consistent comparison between simulated and observed behaviour;
- analysis of representative cislunar scenarios to evaluate visibility, signal strength and navigation performance with and without the lunar beacon.

The rest of the document is structured as follows. Chapter 2 reviews the state of the art in cislunar navigation, including previous research on GNSS-based and hybrid architectures, as well as relevant institutional initiatives. It also summarizes the characteristics and limitations of the pre-existing simulation framework that served as the starting point for this work. Chapter 3 describes the simulation environment and the methodology adopted in this research. It details the extensions introduced in the tool and presents the experimental assessment carried out using real GNSS data. Chapter 4 discusses the results of the simulation campaign performed for the cislunar scenarios defined in this work. The analysis focuses on

the evolution of the received signals along the reference trajectory and concludes with a comparison of the overall navigation performance with and without the beacon. Finally, Chapter 5 summarizes the main conclusions of the study and outlines possible directions for future developments.

Chapter 2

Background and Related Work

In recent years, the problem of navigation in the cislunar environment has received growing attention, leading to a number of studies and initiatives aimed at extending current PNT capabilities beyond Earth orbit. Following the motivations introduced in Chapter 1, this chapter reviews the main studies and technical efforts that provide the foundation for the present work.

The first part outlines the current state of the art in cislunar navigation, covering previous investigations and mission results related to the use of GNSS signals beyond Earth orbit. It also discusses the evolution of hybrid and augmented navigation architectures proposed to improve performance under the challenging conditions of the Earth–Moon environment, together with the most relevant ongoing institutional programs aiming to establish dedicated lunar PNT infrastructures.

The second part describes the simulation framework that served as the starting point for this research. Its main features and limitations are outlined to clarify the motivation for the subsequent methodological extensions presented in Chapter 3.

2.1 State of the Art on Cislunar Navigation

The growing interest in lunar missions has encouraged numerous studies focused on autonomous navigation in the cislunar region. Over the years, both theoretical analysis and experimental activities have contributed to defining the current understanding of how GNSS-based navigation can be achieved beyond Earth orbit. The following section summarizes the main developments that form the background of this work.

2.1.1 Previous Studies and Missions

The use of GNSS for navigation in space has gradually evolved from early experimental demonstrations to practical applications in high-altitude and lunar missions. The first significant milestone dates back to the early 1980s, when the GPSPAC receiver on board Landsat-4 successfully acquired and tracked Global Positioning System (GPS) signals from LEO, proving that satellite-based autonomous navigation was feasible in space [7]. This experiment laid the foundation for the progressive extension of GNSS beyond its original terrestrial domain.

In the late 1990s, several missions began testing GPS reception at higher altitudes. One of the most relevant was ESA's Equator-S mission, launched in 1997, which detected GPS side-lobe signals at altitudes exceeding 60 000 km [16]. These results provided the first direct confirmation that GNSS tracking was possible well beyond the nominal terrestrial service region. Similar outcomes were later obtained by AMSAT-OSCAR 40, confirming that high-sensitivity receivers could exploit weak side-lobe signals even in GEO and Highly Elliptical Orbit (HEO).

These early experiments paved the way for a systematic understanding of GNSS signal behaviour at high altitudes and eventually led to the formal definition of the Space Service Volume (SSV). Coordinated under the United Nations Office for Outer Space Affairs (UNOOSA) in cooperation with all major GNSSs providers, the SSV defines the region of space where GNSS signals can still support navigation and timing functions beyond the nominal terrestrial coverage [17]. It extends from approximately 3 000 km to 36 000 km above the Earth's surface.

Within this volume, signal power and visibility gradually degrade due to the geometry of the transmitting antennas and partial Earth blockage, yet they remain sufficient to enable autonomous orbit determination when multiple constellations are combined. The UNOOSA framework introduced standard performance metrics such as pseudorange accuracy, received power and single and four-signal availability to characterize expected performance in both the lower and upper regions of the SSV. By promoting interoperability across GNSSs constellations, this initiative demonstrated that multi-constellation tracking can significantly improve coverage and reliability at high altitudes, extending the reach of GNSS well beyond its original design intent.

Building on these foundations, research gradually extended toward the possibility of using GNSS signals in cislunar space, beyond the limits of the SSV. In the last decade, several analysis performed by NASA's Jet Propulsion Laboratory (JPL), by the ESA Navigation Support Office [5] and by NASA Goddard Space Flight Center (GSFC) [18] assessed, through high-fidelity simulations, the potential visibility and strength of GNSS signals at lunar distances. These studies showed that, under favorable conditions, a few satellites from multiple constellations could be visible from the near side of the Moon. Although these signals were far below the

thresholds normally used for terrestrial receivers, the analysis confirmed that they could still be exploited for radiometric measurements, orbit determination and timing support when combined with other navigation techniques.

A decisive step forward came with the LuGRE experiment, developed jointly by NASA's Goddard Space Flight Center and the Italian Space Agency (Agenzia Spaziale Italiana (ASI)). The payload, hosted on the Firefly Blue Ghost lander within NASA's Commercial Lunar Payload Services (CLPS) program, was designed to demonstrate the feasibility of acquiring and tracking GPS and Galileo signals during the transfer to the Moon, in lunar orbit and on the lunar surface [19]. Its main objective was to characterize the GNSS signal environment at lunar distances and to evaluate the potential of weak side-lobe signals for navigation and timing.

Following its deployment, LuGRE successfully collected GPS and Galileo measurements throughout its Earth–Moon transit, during orbital operations and after landing [20]. The mission achieved the first direct detection and tracking of GNSS signals at lunar distances, demonstrating that GNSS can be effectively employed to support orbit and timing estimation in the cislunar environment, despite the extremely low received power and challenging geometry.

These achievements marked a significant milestone in the extension of GNSS beyond Earth orbit. Together with the earlier high-altitude experiments and the formal definition of the SSV, the results obtained from LuGRE provided a complete experimental validation of GNSS feasibility in deep-space scenarios. They also laid the technical foundation for future developments, including the design of dedicated lunar navigation infrastructures and hybrid architectures combining GNSS signals with complementary sources.

2.1.2 Ongoing Initiatives for Lunar Navigation

Several international initiatives are currently progressing toward the realization of dedicated infrastructures for lunar communication and navigation. These efforts share a common objective: establishing a persistent and interoperable PNT service that will enable autonomous operations in cislunar space and on the lunar surface.

One of the most advanced initiatives currently under development is the LunaNet architecture, a distributed and extensible framework developed by NASA, ESA and Japan Aerospace Exploration Agency (JAXA) to support future lunar missions with reliable communication, navigation and data exchange capabilities [21]. Developed within the Space Communications and Navigation (SCaN) program, LunaNet is conceived as a "network of networks," enabling both institutional and commercial actors to contribute interoperable nodes to a common infrastructure. The system integrates orbital relays, surface assets and ground stations, all operating under shared protocols and data interfaces, ensuring compatibility across different providers and mission types [22].

LunaNet defines a unified framework for multiple service domains, including communication, navigation, environmental information and science operations. The network relies on Delay/Disruption Tolerant Networking (DTN) to ensure robust and continuous data exchange even under long propagation delays or temporary link disruptions. Its open architecture allows future partners to deploy additional nodes that seamlessly interconnect with existing ones, progressively expanding network coverage around the Moon.

The technical standards and performance requirements are specified in the LunaNet Interoperability Specification (LNIS), maintained by NASA's Goddard Space Flight Center [21]. By promoting international and commercial collaboration, LunaNet establishes the foundation for an integrated communication and navigation ecosystem in cislunar space, supporting the long-term objectives of the Artemis program and future exploration architectures.

The Moonlight programme, developed by the ESA together with an industrial consortium led by Telespazio and supported by the UK and Italian Space Agencies, s the European initiative that aims to provide lunar communication and navigation services in accordance with the LunaNet interoperability specifications. The system, referred to as the Lunar Communications and Navigation Services (LCNS), will comprise a constellation of five satellites in lunar orbit, four dedicated to navigation and one to high-rate data transmission, linked to Earth through three dedicated ground stations [23]. The constellation is optimized to provide coverage of the lunar south pole, where future exploration activities are expected to concentrate. The first element of the programme, the Lunar Pathfinder spacecraft built by Surrey Satellite Technology Ltd. (SSTL), is scheduled for launch in 2026 and will serve as a demonstrator for communication relay operations and for testing GNSS signal reception at lunar distances [23]. The gradual deployment of the full constellation is planned to begin in 2028, reaching operational service by 2030 [23]. Moonlight is being developed in coordination with NASA and JAXA within the LunaNet interoperability framework, ensuring alignment with future global lunar infrastructures [23].

China has also made significant progress in establishing lunar communication and navigation infrastructure through its Queqiao relay satellite system. The first spacecraft, Queqiao-1, was launched in 2018 and placed in a halo orbit around the Earth–Moon L2 Lagrange point, enabling continuous communication between Earth and the far side of the Moon [24]. It played a crucial role in supporting the Chang'e-4 mission [24], which achieved the first landing on the lunar far side in January 2019 [25]. In March 2024, China successfully launched Queqiao-2, a larger and more capable relay satellite operating in a frozen elliptical lunar orbit, designed to provide coverage for the entire lunar surface. Queqiao-2 is part of a broader plan for a future Queqiao constellation, which will expand the system's functionality beyond communication to include navigation and remote-sensing services [26].

The private sector is also taking an active role in the development of lunar communication and navigation infrastructures. One of the most prominent initiatives is Lockheed Martin's Parsec network, operated by its subsidiary Crescent Space Services. Conceived as a commercial, service-oriented system, Parsec will consist of a constellation of small satellites placed in lunar orbit to provide continuous communication links between the Earth, orbiting assets and surface operations [27]. In addition to data relay functions, the system will offer positioning and timing services, effectively acting as a lunar analogue of terrestrial GNSS [27]. Parsec is designed to interoperate with emerging international frameworks such as LunaNet, contributing to the establishment of a resilient, commercially driven infrastructure for the future lunar economy [27].

Collectively, these initiatives demonstrate a global effort toward the establishment of interoperable and sustainable PNT services for the Moon. The convergence of governmental programs and commercial ventures marks a decisive step toward the creation of a permanent cislunar infrastructure. These developments will not only enhance autonomy and safety for future missions but will also lay the groundwork for a broader lunar economy based on shared standards and cooperative architectures.

2.2 Pre-Existing Simulation Framework and Limitations

At the beginning of this research, a dedicated simulation environment was already available and served as the starting point for the analysis presented in this work [14, 28]. The framework was conceived to emulate the reception of GNSS signals by a spacecraft operating beyond Earth orbit and to evaluate the achievable navigation accuracy under realistic conditions. It combines orbital mechanics, antenna modelling, radiometric analysis and navigation filter testing into a single MATLAB-based environment. Before introducing the extensions and methodological updates developed in this thesis, this section provides a comprehensive overview of the pre-existing framework and summarizes its main characteristics, assumptions, and design objectives.

2.2.1 Overview of the Simulation Environment

The simulation framework was designed to reproduce, with high fidelity, the behaviour of a GNSS receiver operating along a representative Earth-Moon transfer trajectory. All computations are performed within an Earth-Centered, Earth-Fixed (ECEF) reference frame, in which the Earth, Moon and Sun are modelled as celestial bodies with their relative positions and motions updated at each simulation epoch.

The receiver motion is defined by a reference Earth–Moon transfer trajectory provided as a time-tagged sequence of spacecraft positions and velocities in the ECI J2000 frame. After conversion into the ECEF frame, the trajectory is interpolated to obtain a uniform 1-Hz sampling, which allows a consistent evaluation of visibility and link-budget parameters along the transfer. In parallel, the GNSS satellites, belonging to the GPS and Galileo constellations, are propagated using broadcast ephemerides extracted from reference navigation files.

The tool follows a modular design, allowing the user to configure each simulation through a set of control parameters defining the time step, number of epochs, active constellations and processing algorithms. Two operational modes are implemented: a coarse, mission-wide analysis with reduced temporal resolution (typically one snapshot every 15 minutes) and a high-fidelity local analysis of selected mission phases with one-second granularity. This dual approach makes it possible to balance computational cost with temporal accuracy, depending on the study objective.

At the core of the simulator lies a receiver-satellite link model, which computes for each epoch the geometric visibility and radiometric detectability of every satellite in view. Geometric visibility is determined by verifying that the line of sight between the spacecraft and the satellite is not blocked by the Earth or the Moon, while radiometric visibility is based on the predicted C/N_0. The C/N_0 is derived from a link budget model including the satellite's transmitted power, the antenna gains of both transmitter and receiver, free-space losses, polarization and receiver losses, and system noise temperature. A configurable C/N_0 threshold is then applied to determine whether a signal can be tracked by the receiver at a each epoch.

The receiver model emulates a high-sensitivity GNSS payload for deep-space operations. The antenna is represented by a directional pattern defined on the same azimuth/co-elevation grid used for transmit models. In the baseline tool the pattern is intentionally simple and band-agnostic: it features a single main lobe aligned with the boresight, a peak gain of 15–16 dBi, and a smooth off-boresight roll-off without pronounced side-lobe structure (see Fig. 2.1). The receiver clock is represented with a simple two-state stochastic model, bias and drift, that evolve as a random walk. This produces a common time error across simultaneous measurements and a slowly varying frequency offset, yielding realistic perturbations on pseudorange and Doppler.

On the transmitter side, each GNSS satellite is represented as an independent object characterized by its position, velocity, antenna pattern and transmitted power. The simulator supports multiple satellite blocks for GPS (IIR, IIR-M, and IIF) and a generic model for Galileo. For each satellite, the simulator determines the relative azimuth and elevation angles of the spacecraft within the satellite's body-fixed reference frame and interpolates the corresponding antenna gain. This approach ensures a realistic evaluation of signal power variation with respect to off-boresight angles and spacecraft attitude.

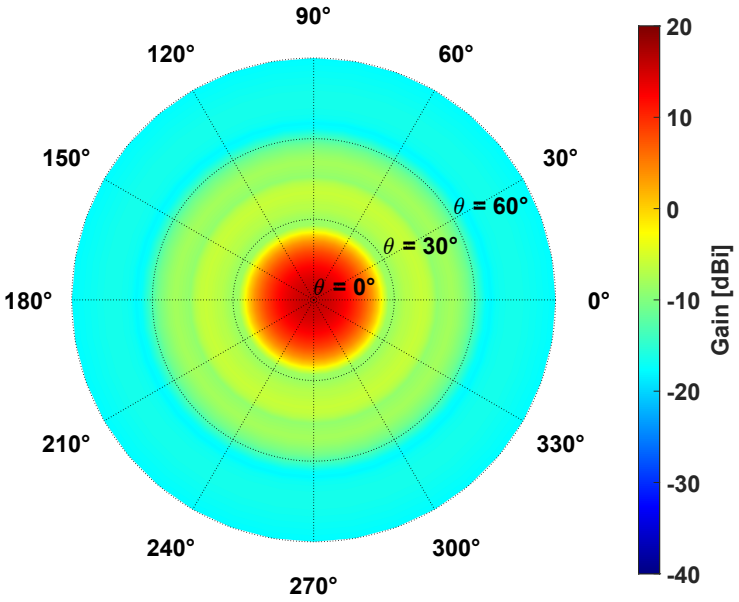

Figure 2.1: Polar representation of the receiver antenna gain used in the baseline simulator.

Based on the predicted signal strength, the simulator generates synthetic GNSS observables, including pseudoranges, pseudorange rates, Doppler shifts and Doppler rates. Measurement noise is added as zero-mean Gaussian noise, whose standard deviation is modelled as a function of the instantaneous C/N_0 according to the curves presented in the LuGRE analysis [29]. The noise standard deviation models for the pseudorange and the Doppler shift were reconstructed starting from a generic exponential function

$$f(x) = a\, b^{(x-x_0)} + c \tag{2.1}$$

where the parameters a, b, x_0, c are chosen differently for pseudorange and Doppler observables to best reproduce the shapes of the corresponding reference curves [29]. The observables are computed for each Monte Carlo realization, allowing the statistical characterization of estimation errors and filter stability. The observables are computed for each Monte Carlo realization, allowing the statistical characterization of estimation errors and filter stability.

The navigation solution is estimated through a configurable Position, Velocity, Time (PVT) processing engine. The framework includes:

- **Least-Mean-Squares (LMS)**: provides an initial coarse solution from the available observables.

- **Extended Kalman Filter (EKF)**: performs recursive state estimation relying solely on GNSS measurements.

- **Trajectory-Aware Extended Kalman Filter (TA-EKF)**: integrates external trajectory information as an aiding input to improve robustness in weak-signal or poor-geometry conditions [14].

Each filter is executed across multiple Monte Carlo runs to assess convergence and steady-state accuracy. The modular structure of the framework allows these algorithms to be activated independently, facilitating performance comparisons under identical simulation conditions.

The overall workflow is organized around the central routine that iterates over all epochs, updating the positions of the Sun, Moon and satellites, computing visibility, generating measurements and feeding them to the chosen navigation filter. At the end of the simulation, all relevant quantities, such as visibility maps, link budgets, satellite geometry, estimated trajectories and C/N_0 time histories, are stored for post-processing and visualization. This design enables a comprehensive evaluation of GNSS signal availability and navigation performance for space missions extending well beyond traditional Earth-orbiting regimes.

2.2.2 Identified Limitations and Need for Extensions

The original simulator was a solid base for exploring GNSS performance along an Earth–Moon transfer, but a few choices in scope and modelling limited how far its results could be generalized. The most obvious constraint was constellation coverage. By handling only GPS and Galileo, the planner could not account for the contribution of additional systems that become increasingly relevant as the link budget tightens with distance. Under cislunar conditions, the number of usable signals at any given epoch can be small and geometry changes quickly. Relying on only two constellations risks missing periods where the combined availability of several systems would keep the solution well-conditioned.

Transmitter modelling also needed to be brought to a consistent level of detail. GPS satellites were already described by realistic antenna patterns, while the Galileo space segment was represented by a simplified pattern. That asymmetry can bias radiometric predictions, particularly at large off-boresight angles where small differences in the antenna gain may lead to meaningful variations in received power.

Frequency coverage was another limitation. The original configuration considered only the L1/E1 band. While acceptable for an initial study, a single-band setup reduces completeness and prevents a balanced comparison across constellations and services. Extending the analysis to multiple bands improves representativeness

and supports multi-constellation assessments without relying on band-specific assumptions.

The modelling scope also excluded hybrid PNT options. By assuming GNSS-only operation, the simulator could not be used to explore architectures that rely on auxiliary infrastructure to extend coverage in cislunar space. In particular, the absence of a lunar beacon model prevented any assessment of coverage enhancement, handover continuity or the performance improvements that a beacon might provide compared to GNSS-only baselines.

From a data-handling perspective, the baseline tool did not provide a mechanism to ingest navigation data directly from external Receiver Independent Exchange Format (RINEX) files. Constellation geometry and timing were derived from pre-packaged inputs within the tool, which simplified execution but reduced flexibility for tailoring scenarios to specific epochs or for aligning the simulation to external references. Moreover, prediction outputs, such as satellite visibility, had not been cross-checked against visibility data obtained from real receivers, leaving the representativeness of simulated visibility unverified with respect to actual conditions.

Taken together, these constraints, restricted constellation and band coverage, uneven transmitter modelling for Galileo, absence of hybrid elements, reliance on pre-packaged inputs without RINEX ingestion and lack of external visibility verification, motivated the extensions described in Chapter 3.

Chapter 3

Methodology: Simulation Framework Design and Assessment

Building on the requirements and limitations identified in Section 2.2.2, the original simulator was adapted and expanded to meet the needs of this study. The starting environment did not provide the necessary constellation coverage, antenna modelling detail, or augmentation elements required for a representative analysis of radionavigation in cislunar space. This chapter explains how the tool was extended and reorganized. First, the existing modelling of GPS and Galileo was refined, in particular in terms of antenna patterns and frequency coverage. Then, several new modules were developed, including the integration of additional GNSS and regional constellations and the implementation of a lunar surface radio-beacon transmitting in a GNSS frequency band.

The extended framework was experimentally validated through a comparative analysis between predictions and real GNSS observations collected using a Septentrio receiver, focusing on satellite visibility and timing consistency.

Finally, the chapter introduces the navigation scenarios defined for cislunar environment, featuring different configurations of the lunar beacon and receiver antenna pointing. The simulated receiver follows a predefined trajectory representative of a spacecraft performing an Earth–Moon transfer, providing a realistic context for assessing GNSS availability and evaluating the potential benefits of lunar augmentation along the mission profile.

3.1 Extensions to the Existing Simulation Tool

The original configuration of the simulator included only the GPS and Galileo constellations, with a simplified radiometric characterization and a single frequency band configuration. As a first step, the existing modelling of these systems was refined to obtain a more realistic description of the transmitted power and directional gain, while preserving the overall structure of the original tool. This involved introducing a multiple frequency bands and updating the antenna patterns used for GPS and Galileo signals.

3.1.1 Integration of Realistic Antenna Patterns

To support a more detailed radiometric characterization of GPS and Galileo signals, the corresponding antenna models were updated to include all the main operational frequency bands, with dedicated gain distributions whenever available. Table 3.1 summarizes the frequency bands currently modelled for the two constellations.

Constellation	**Frequency Bands**	**Nominal f_c [MHz]**
GPS	L1, L2, L5	1575.42, 1227.60, 1176.45
Galileo	E1, E5a, E5b, E6	1575.42, 1176.45, 1207.14, 1278.75

Table 3.1: Frequency bands modelled for GPS and Galileo.

GPS Antenna Patterns

The simulation environment includes realistic antenna radiation patterns for the GPS constellation over the main operational blocks currently in service: IIR, IIR-M and IIF. These patterns were already present in the simulator and were originally derived from publicly available technical data [30]. Each satellite is associated with a gain pattern defined over a discretized azimuth and co-elevation grid, allowing the simulator to take into account the effects of side-lobe signal attenuation and off-boresight signal reception.

In the default simulator configuration, a specific satellite model is assigned to each GPS satellite slot, with an associated nominal transmit power and antenna gain matrix. The original gain matrices were provided in terms of Directivity and the corresponding antenna gain is obtained by applying a gain correction factor (GCF) to the Directivity values. A summary of the transmit power levels and GCFs used for each satellite block is reported in Table 3.2.

The available transmit antenna patterns for GPS refer to the L1 band. Since band-specific patterns for L2 and L5 were not available, the same pattern used

Satellite Block	Transmit Power [dBW]	GCF [dB]
IIR	17.3	0.7–1.4
IIR-M	18.8	1.1–1.4
IIF	16.2	1.0 (assumed average)

Table 3.2: Transmit power and GCF used for GPS antenna patterns

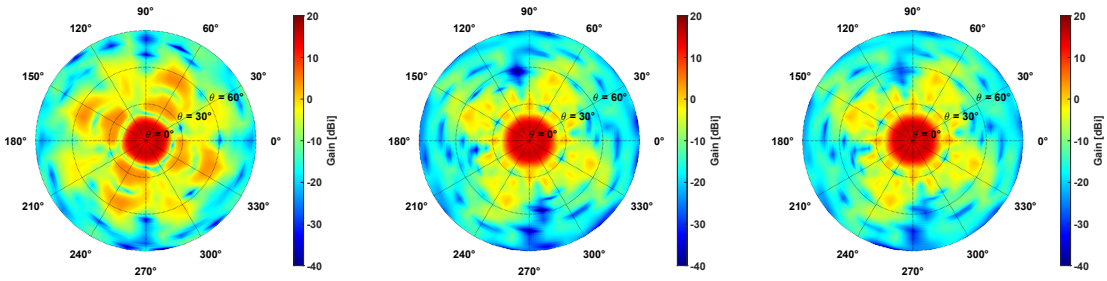

(a) GPS IIR (b) GPS IIR-M (c) GPS IIF

Figure 3.1: Polar antenna gain patterns for the main GPS satellite blocks: IIR, IIR-M and IIF.

for L1 was reused for these bands. In practice, a band-invariant pattern shape is adopted. This modelling choice avoids introducing unsupported extrapolations and maintains consistency in the radiometric treatment across frequencies. Its implications are analyzed in the next chapter.

Galileo Antenna Patterns

In the initial configuration of the simulator, the antenna radiation pattern of the Galileo constellation was represented by a simplified, coarse model. The pattern was approximated by a stepwise approximation of side lobes and the main lobe, intended to reproduce an average trend over the constellation. It was defined over a limited number of angular intervals and constant gain values were assigned to each segment, creating sharp transitions between angular sectors.

While this representation allowed easy visibility and gain analysis, it lacked the resolution and smoothness required to capture more detailed effects, such as gradual off-boresight attenuation or precision side-lobe reception. The pattern introduced gain discontinuities in computations and was not appropriate for high-fidelity link-budget or signal availability calculations.

To overcome these limitations, the simulator was upgraded to incorporate a more

realistic and detailed antenna pattern model for Galileo signals. This updated model is based on the Galileo Reference Antenna Pattern (GRAP) dataset developed by the Joint Research Centre (JRC), which provides a high-resolution estimate of the Effective Isotropic Radiated Power (EIRP) over a dense azimuth and co-elevation grid [31].

The raw GRAP data were provided in the form of a 361×91 EIRP matrix covering azimuth angles from 0° to 360° and co-elevation angles between 0° and 90°, i.e., the forward hemisphere of the transmit antenna. Since no public characterisation is available for negative co-elevations and the radiation in that region is several tens of decibels weaker, the pattern was extended by mirroring the available data to obtain a complete $[-90^\circ, 90^\circ]$ coverage. This is a standard approach when only the forward portion of the pattern is provided and ensures a continuous gain surface without introducing arbitrary features in the back-lobe region. The resulting matrix was finally interpolated onto the simulation grid, defined by a 2° step in co-elevation and 10° in azimuth, to obtain a smooth and numerically consistent antenna gain surface.

The gain pattern was obtained by subtracting a nominal transmitted power value from the interpolated EIRP, according to the well-known relationship:

$$\mathrm{EIRP}_{f,\mathrm{dBW}}(\theta, \phi) = P_{t,f,\mathrm{dBW}} + G_{f,\mathrm{dBi}}(\theta, \phi) \tag{3.1}$$

where P_t is the transmit power and $G(\theta, \phi)$ the directional antenna gain. A transmit power of 14.5 dBW was adopted, in accordance with values reported in recent link-budget analysis for Galileo Full Operational Capability (FOC) satellites [32].

The final antenna pattern model enabled a far more realistic evaluation of visibility, gain and signal strength throughout the simulated spacecraft trajectories, significantly improving the physical accuracy of link-budget computations for Galileo-based navigation in cislunar scenarios.

This improvement is clearly visible in Figure 3.2, where the realistic GRAP-based pattern displays smooth angular transitions and well-shaped side lobes, in contrast to the segmented gain blocks of the simplified model.

Unlike the GPS case, for Galileo the reference dataset provides band-dedicated transmit patterns. In this work, realistic patterns are adopted for all bands used in the analysis, namely E1, E5a, E5b and E6 (shown in Figure 3.3). Each band is processed on its own azimuth/co-elevation grid and kept separate in the simulator, so that band-dependent angular features are preserved without reusing the E1 pattern across frequencies. The same interpolation workflow described above is applied to each band to obtain smooth gain surfaces suitable for link-budget computations.

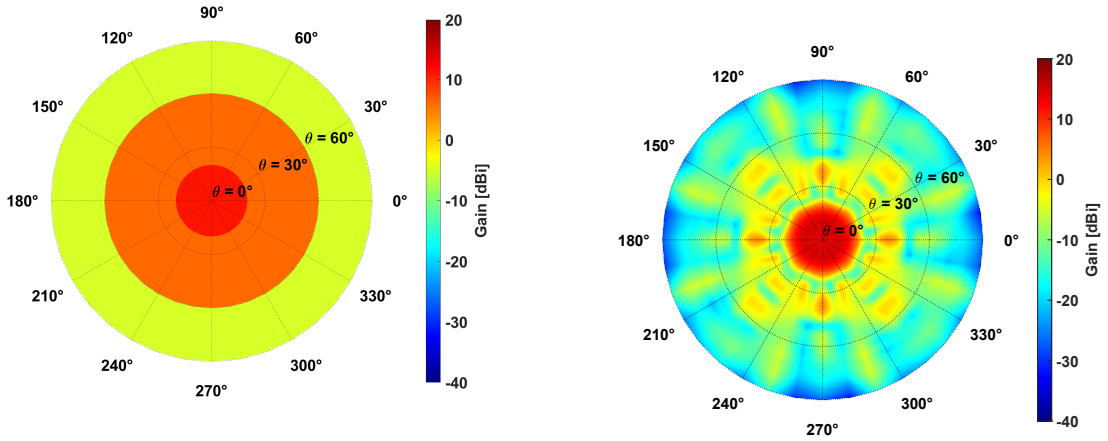

(a) Simplified antenna pattern **(b)** Realistic antenna pattern

Figure 3.2: Polar representation of Galileo E1 antenna gain.

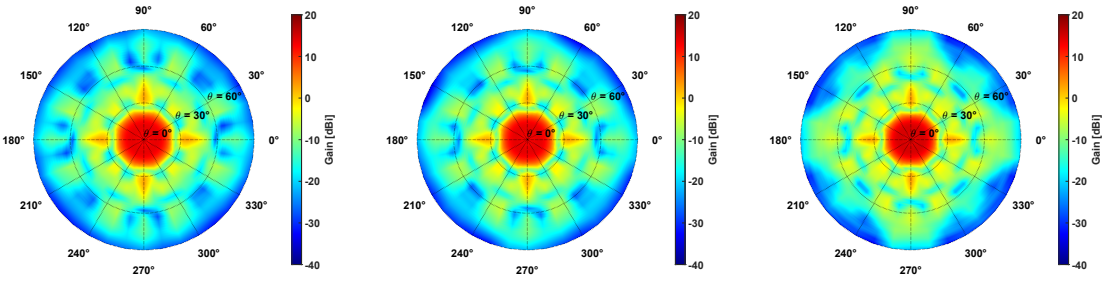

(a) E5a **(b)** E5b **(c)** E6

Figure 3.3: Realistic transmit antenna gain for Galileo bands E5a, E5b and E6.

3.2 Capabilities Introduced in the Simulation Tool

In addition to the refinements applied to the existing constellations, several new capabilities were introduced as part of this work. These extensions significantly broaden the scope of the simulator, enabling multi-constellation analysis and the inclusion of a lunar augmentation element. The main additions are related to the support of additional GNSS and regional systems and the implementation of a configurable lunar surface beacon.

3.2.1 Inclusion of Multiple GNSS Constellations

The simulator has been extended to include all major global and regional navigation systems. This enhancement not only improved completeness but also allowed for more realistic and flexible simulations, particularly in studies requiring a broader and more representative satellite geometry. In addition to GPS and Galileo, the updated environment now also supports GLONASS, BeiDou, Quasi-Zenith Satellite System (QZSS) and Indian Regional Navigation Satellite System (IRNSS). This extension allows the user to configure the desired combination of constellations for any given simulation scenario, enabling both single-system and multi-constellation analysis.

Table 3.3 summarizes the frequency bands modelled for the newly added systems.

Constellation	**Bands Included**	**Nominal f_c [MHz]**
GLONASS	L1	1575.42
BeiDou	B1C, B2a	1575.42, 1176.45
QZSS	L1, L2, L5	1575.42, 1227.60, 1176.45
IRNSS	L5	1176.45

Table 3.3: Frequency bands modelled for the newly added constellations.

For several of these constellations, band-specific transmit patterns are not publicly available. In such cases, the same angular gain distribution is applied across all the modelled bands of that constellation. This conservative choice avoids unsupported extrapolations and keeps the radiometric treatment consistent.

The implementation of this feature required the integration of real ephemeris data for multiple systems. Navigation parameters are imported from RINEX navigation files corresponding to the simulation epoch, ensuring consistency with the actual orbital configuration at the time of interest. For each constellation the function `gnssconstellation()` computes the satellite positions and velocities based on broadcast ephemeris, while the simulation environment generates dynamically a set of `Satellite` objects. These objects include all the relevant properties, including constellation membership, orbital state and the parameters used in the subsequent visibility and link-budget computations.

A constellation-specific note applies to GLONASS. The behaviour of the function `gnssconstellation()` follows the constellation-specific validity windows, which are much narrower for GLONASS than for other systems [33]. In practice, GLONASS broadcast parameters are considered accurate only within a short interval around the time of ephemeris (±15 minutes), whereas GPS, Galileo, BeiDou, IRNSS and QZSS are typically valid over wider windows (about ±2 hours). To respect this constraint, GLONASS states are propagated only within a short time window

around the epoch of interest and additional checks are applied to discard any out-of-window states before they enter the visibility and link-budget pipeline. Other constellations are evaluated over their broader validity intervals with the usual ephemeris checks.

The initialization process is entirely modular: each constellation is handled by a dedicated block within the simulator and can be selectively enabled or disabled through user-defined parameters. All initialized satellites are aggregated into a single structure, enabling a common processing chain for visibility checks, C/N_0 estimation and performance evaluation.

QZSS Antenna Patterns

As part of this work, support for the QZSS was integrated into the simulation framework. Unlike GPS or Galileo, the simulator did not previously include any QZSS antenna models. In order to address this, publicly available directional gain data, released by the Japanese Cabinet Office in 2023 for all operational satellites (QZS-1R to QZS-7), were imported and processed to enable accurate modelling of the signal transmission patterns [34].

The antenna patterns were supplied as tables of gain values expressed in dBi, each defined at specific combinations of azimuth and co-elevation angles. However, their angular coverage and resolution varied significantly across satellites. In particular:

- the co-elevation angle (θ) was defined only up to 60° in most cases, while others reached 90°;
- the azimuth (ϕ) was sampled either at 30° intervals (12 points from 0° to 330°) or at 10° intervals (36 points from 0° to 350°).

To ensure consistency within the simulation engine, all raw patterns were symmetrically extended to negative co-elevation angles (covering $[-90°, +90°]$) and interpolated onto the standard simulation grid, defined by a 2° step in θ and 10° in ϕ. When the original pattern ended at 60°, a linear attenuation scheme was applied to smoothly extrapolate the pattern up to 90°. Specifically, the last available co-elevation profile ($\theta = 60°$) was gradually blended, over uniform steps, with the minimum gain value found in the original matrix (see e.g., Figure 3.4 (a)). This approach ensured a realistic angular decay without introducing artificial discontinuities or overly optimistic signal coverage in high off-nadir directions.

Similarly, when the azimuth range did not reach 360°, the first column was duplicated to close the circular domain, guaranteeing continuity in azimuthal interpolation. A detailed summary of the original angular coverage and required modifications for each QZSS satellite is reported in Table 3.4.

Satellite	**Original θ Range**	**Original ϕ Range**	**Adjustments**
QZS-1R	0°–60°	0°–350° (10° step)	Extended in θ
QZS-2	0°–60°	0°–330° (30° step)	Extended in θ, ϕ padded to 360°
QZS-3	0°–60°	0°–330° (30° step)	Extended in θ, ϕ padded to 360°
QZS-4	0°–60°	0°–330° (30° step)	Extended in θ, ϕ padded to 360°
QZS-5	0°–90°	0°–350° (10° step)	None
QZS-6	0°–90°	0°–350° (10° step)	None
QZS-7	0°–90°	0°–350° (10° step)	None

Table 3.4: Original angular sampling of QZSS antenna gain patterns

The QZSS pattern files used in this work provide per-satellite, multi-band data, with one worksheet per frequency band (L1, L2, L5). Patterns for L1 and L5 were available for all spacecraft (QZS-1R to QZS-7), whereas L2 was not provided for QZS-5, QZS-6 and QZS-7. In order to avoid unsupported extrapolations, when an L2 pattern was missing, the corresponding L1 angular distribution was reused for L2 for the same satellite. Each band was processed independently on its original angular grid and mapped to the simulator's reference grid using the same extension/interpolation workflow described above.

Each QZSS satellite was then associated with its own processed gain matrix and assumed to transmit with a nominal power of 14.5 dBW. The resulting models allow realistic evaluation of direction-dependent signal strength and visibility in simulations involving high-altitude or lunar-bound spacecraft (see Figure 3.4 for the processed antenna patterns).

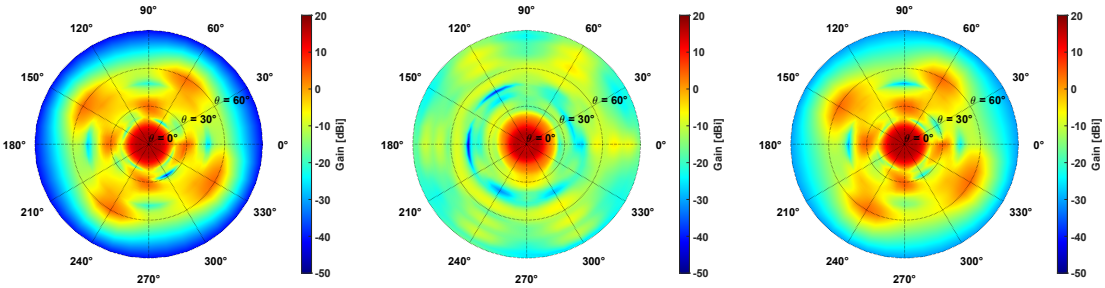

(a) QZS-1R (b) QZS-2 (c) QZS-3

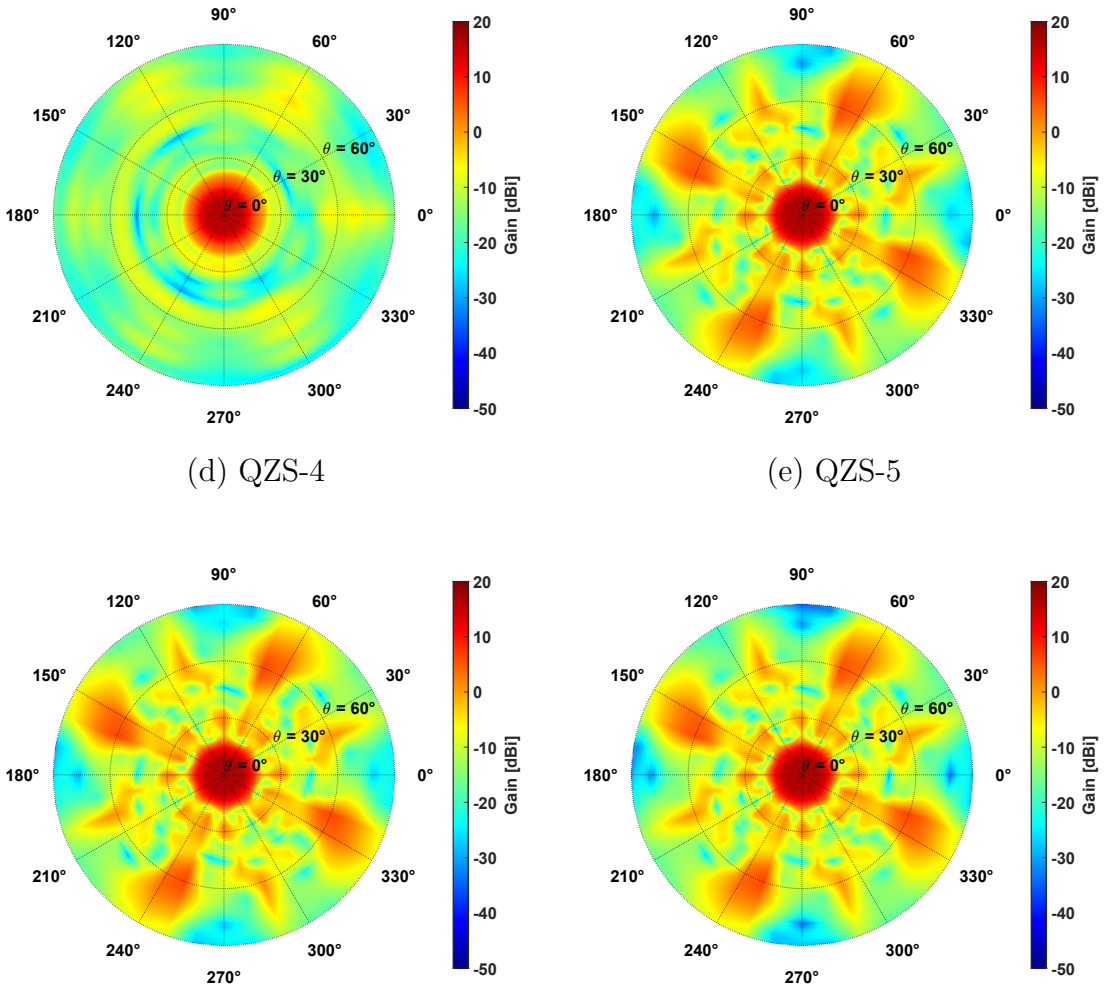

(d) QZS-4 (e) QZS-5

(f) QZS-6 (g) QZS-7

Figure 3.4: QZSS antenna patterns for the L1 frequency band.

GLONASS, BeiDou and IRNSS Antenna Patterns

At the time of this work, no official directional antenna gain patterns were publicly available for the GLONASS, BeiDou or IRNSS constellations in a format compatible with the simulation framework. In the absence of such models, it was necessary to adopt a surrogate approach in order to enable visibility and signal strength analysis involving these systems.

For that reason, the simulator reuses the antenna pattern associated with GPS slot 1, corresponding to satellite SVN65 of Block IIF (Fig. 3.5). This pattern was

selected for its neutral and well-behaved radiation profile, which includes realistic off-boresight attenuation and lacks aggressive side lobes. Among the available GPS models integrated in the simulator (Blocks IIR, IIR-M, and IIF), the Block IIF pattern offers a balanced compromise between simplicity and realism, making it a suitable placeholder for constellations lacking official antenna data.

Since it was not available a band-dedicated transmit pattern for this surrogate satellite, the same angular distribution was reused across all bands considered for each constellation, which are listed in Table 3.3.

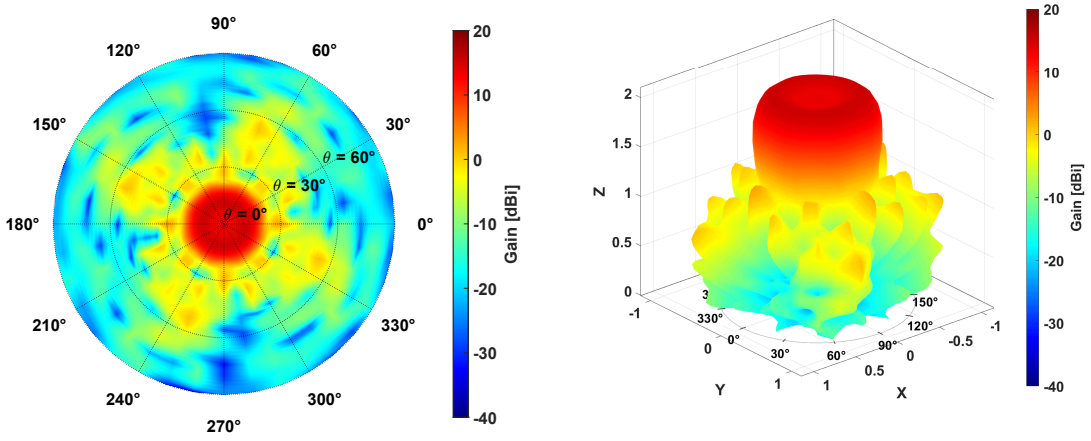

(a) 2D polar projection

(b) 3D gain representation

Figure 3.5: Surrogate antenna pattern (GPS Block IIF – SVN65) used for GLONASS, BeiDou and IRNSS in the absence of official data.

This approach maintains consistency across all GNSS constellations considered and avoids idealized approximation and excessively pessimistic signal models. Although it does not reflect the specific transmission characteristics of GLONASS, BeiDou or IRNSS satellites, it enables coherent multi-GNSS simulations and provides a conservative basis for link-budget computations. The simulator is designed to accommodate future replacement with more accurate patterns as soon as they become available.

3.2.2 Modelling of Lunar Beacon

A dedicated model of a *lunar beacon* was developed and integrated to enable the analysis of hybrid GNSS-based navigation in cislunar space. The beacon acts as a signal source positioned on the Moon's surface, designed to simulate a potential augmentation element transmitting GNSS-like signals. This feature was included to simulate scenarios where signal geometry and availability are improved by the

presence of a fixed lunar transmitter.

The beacon was implemented as a dedicated MATLAB class, `LunarBeacon`, which defines its position on the lunar surface, the associated local reference frame, its orientation, and its radiative behavior. Its position is computed as a fixed offset from the centre of the Moon, along a defined direction (typically toward Earth) and scaled to the Moon's radius, ensuring that the beacon is consistently placed on the lunar surface.

To clarify the pointing geometry, the orientation of the beacon can be described in simple analytical terms. Let $\mathbf{r}_\mathrm{b}$ be the beacon position and $\mathbf{r}_\mathrm{t}$ the target point. The antenna boresight direction is defined by the unit vector

$$\hat{\mathbf{z}}_\mathrm{b} = \frac{\mathbf{r}_\mathrm{t} - \mathbf{r}_\mathrm{b}}{\|\mathbf{r}_\mathrm{t} - \mathbf{r}_\mathrm{b}\|} \tag{3.2}$$

while the remaining axes of the local frame are obtained by orthogonal completion using a secondary reference direction to avoid degeneracies. The Line of Sight (LOS) to a receiver at position $\mathbf{r}_\mathrm{rx}$ is then projected into this local frame and converted into the corresponding azimuth and co-elevation angles used to query the antenna pattern. This formulation reflects the geometric steps implemented in the simulator.

The radiative characteristics of the beacon are defined through an antenna pattern inherited from the existing GNSS satellite models available in the simulator (Figure 3.6). This choice allows the beacon to adopt a realistic, direction-dependent transmission gain without introducing overly idealized assumptions and represents a practical way to model the beacon by taking a GNSS transmit payload as a first reasonable reference. The gain towards a target is calculated by projecting the relative vector into the local antenna frame of the beacon and interpolating the gain value from the pattern matrix.

The antenna orientation is defined by a local coordinate system constructed at each simulation epoch. The z-axis of the frame is directed toward a target point: either the centre of Earth or the spacecraft, depending on the scenario under analysis. Two pointing modes are considered: one with a fixed pointing direction toward Earth and one with dynamic pointing that continuously tracks the receiver. These configurations represent two realistic mission concepts, a passive Earth-pointing beacon and an active reciprocal-link system.

The beacon model is fully integrated in the simulation environment and participates in every epoch computation. It provides its antenna orientation and gain, contributes to the link budget evaluation and enables the computation of received signal strength at the spacecraft location. The resulting parameters like distance, antenna gains, line-of-sight angle to the main lobe, are recorded and used later for further quantitative analysis of signal availability.

In addition to the forward link budget used to estimate the received signal strength at the spacecraft, the beacon model also supports an inverse link-budget

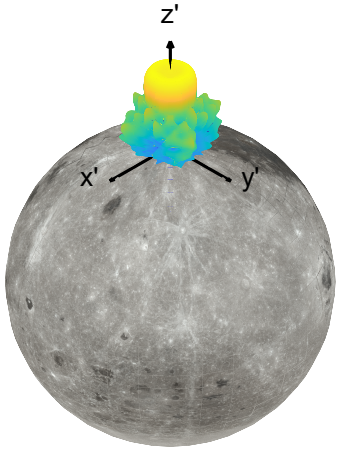

Figure 3.6: 3D visualization of the lunar beacon antenna pattern projected outward from the Moon's surface.

analysis. This complementary computation determines the maximum transmit power that the beacon could radiate toward Earth without exceeding a predefined interference threshold for GPS L1 signals at the Earth's surface. This functionality enables the assessment of regulatory and compatibility constraints for the beacon and the identification of the most restrictive operating conditions in each scenario. The methodology and results of this analysis are presented in Chapter 4.

3.3 Experimental Assessment with Real GNSS Data

In order to evaluate the accuracy of the simulator, a validation experiment was performed based on real data collected from a high-precision, multi-constellation GNSS receiver. The objective was to verify whether the satellite visibility predicted by the simulation environment, using only broadcast ephemerides and a known observation point, matched the actual satellites observed from Earth during the same time period. This comparison allowed to assess the reliability of the planner under realistic conditions and to detect any potential discrepancies in the predicted start and end times of visibility windows.

While this comparison is useful as a consistency check, it is naturally limited with respect to the cislunar environment considered in the thesis. At the moment, there are no publicly accessible GNSS measurements acquired at lunar distances. LuGRE is the only mission that has demonstrated GNSS reception in that region, but its data are not openly accessible, so they cannot be used for validation. For this reason, the comparison was carried out using a terrestrial dataset, which allows

a direct match between the simulator outputs and real observations under standard reception conditions.

These conditions are clearly different from those encountered in deep space, where the received power is much lower and dominated by sidelobe contributions. The results shown here should therefore be interpreted only as a way to verify that the visibility planner behaves consistently when compared with real data on ground. Once this consistency is established, the simulator can be reliably applied to the lunar-transfer trajectory analysed in the following sections.

3.3.1 Experimental Setup

The reference dataset for this analysis was acquired on April 22$^{\text{nd}}$, 2025 (112th day of the year), using high-end Septentrio receiver connected to a georeferenced Leica AR20 antenna installed on the roof of the Department of Electronics and Telecommunications building at Politecnico di Torino. The observation point was characterized by the following World Geodetic System 1984 (WGS84) coordinates, also shown in Figure 3.7:

- **Latitude:** 45° 03′ 51.8968″ N
- **Longitude:** 7° 39′ 43.0717″ E
- **Ellipsoidal height:** 322.3106 m

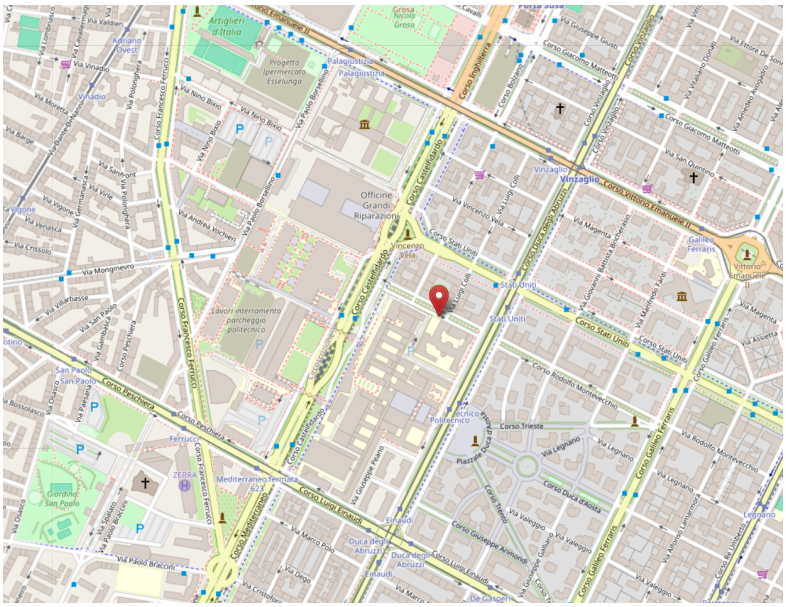

Figure 3.7: Antenna mounting point at Politecnico di Torino (Italy), equipped with a Leica AR20 geodetic antenna used for the real GNSS data collection.

Throughout the entire day, a high-performance Septentrio PolaRx5S receiver (Figure 3.8) was used to collect raw GNSS data at high resolution. The data were later organized into 15-minute RINEX-formatted segments, producing two types of files per interval: a `.250` file containing raw observation data (e.g., pseudorange, carrier phase, Doppler) and a `.25P` file containing ephemeris and visibility information as internally processed or predicted by the receiver itself. In parallel, a broadcast navigation RINEX file was obtained from the International GNSS Service (IGS) repository. This file, valid for the same date, included ephemerides for both the GPS and Galileo constellations and was used to generate ideal satellite predictions within the simulation environment.

Figure 3.8: Septentrio PolaRx5S GNSS receiver used for the data collection, supporting multiple frequencies and constellations..

The assessment focused on a selected 6-hour window, from 09:00 to 15:00 UTC. Each 15-minute block was processed independently and the satellite visibility was reconstructed from three distinct sources:

1. **Real visibility**, obtained directly from the receiver's `.250` file. This reflects the satellites that were actually tracked at each epoch and serves as the experimental ground truth.

2. **Simulated visibility**, computed using the broadcast navigation file and the known receiver location. This prediction represents the ideal conditions expected from a planner using only official orbital information and standard models of satellite motion and visibility.

3. **Receiver-predicted visibility**, extracted from the `.25P` file, which contains ephemerides internally filtered and interpreted by the Septentrio receiver.

A comprehensive comparison was then performed. For each satellite observed or predicted, the system computed the following performance metrics:

- ΔStart: the time difference between predicted and real visibility start times,

- ΔEnd: the time difference in visibility end times,
- ΔDur: the difference in total visibility duration,
- Overlap (%): the percentage of temporal overlap between predicted and observed visibility intervals.

These metrics were computed separately for both the simulation based on the official navigation file and for the `.25P`-based receiver prediction. All the results were aggregated across all time intervals into structured datasets for further analysis. The output included both a comprehensive visibility table and a performance error table indexed by satellite PRN and source.

In addition to the visibility windows, elevation angle profiles were also computed and stored. This allowed for a visual comparison of how the simulated and predicted satellite trajectories matched the actual observed ones over time, offering further insight into the accuracy of the planner's geometric predictions.

By consolidating the results across the 6-hour test window, the system produced a global visibility summary that enabled both qualitative and quantitative validation of the GNSS visibility planner.

3.3.2 Validation Results

Using the three visibility sources defined in the previous subsection, the validation focused on how well the predicted visibility intervals reproduce the actual tracking recorded by the receiver over the six-hour observation window. A first, qualitative comparison was carried out by analysing a Gantt-style chart that summarizes the visibility timelines for each satellite over the full observation window.

Figure 3.9 provides an overview of the visibility intervals for all satellites observed during the six-hour session. Each satellite is represented by a horizontal sequence of coloured bars, where different colours indicate different sources of visibility information:

- Blue bars represent the actual satellite visibility recorded by the receiver in the RINEX observation file (.25O), used as the reference dataset.
- Green bars correspond to the visibility predicted by the simulation tool, based on broadcast ephemerides from the RINEX Navigation message (NAV) message.
- Red bars show the visibility predicted internally by the Septentrio receiver and recorded in the .25P file, which includes precomputed tracking forecasts.

Beyond the overall agreement visible in the Gantt chart, minor differences can be observed in the visibility intervals between the three data sources. These variations

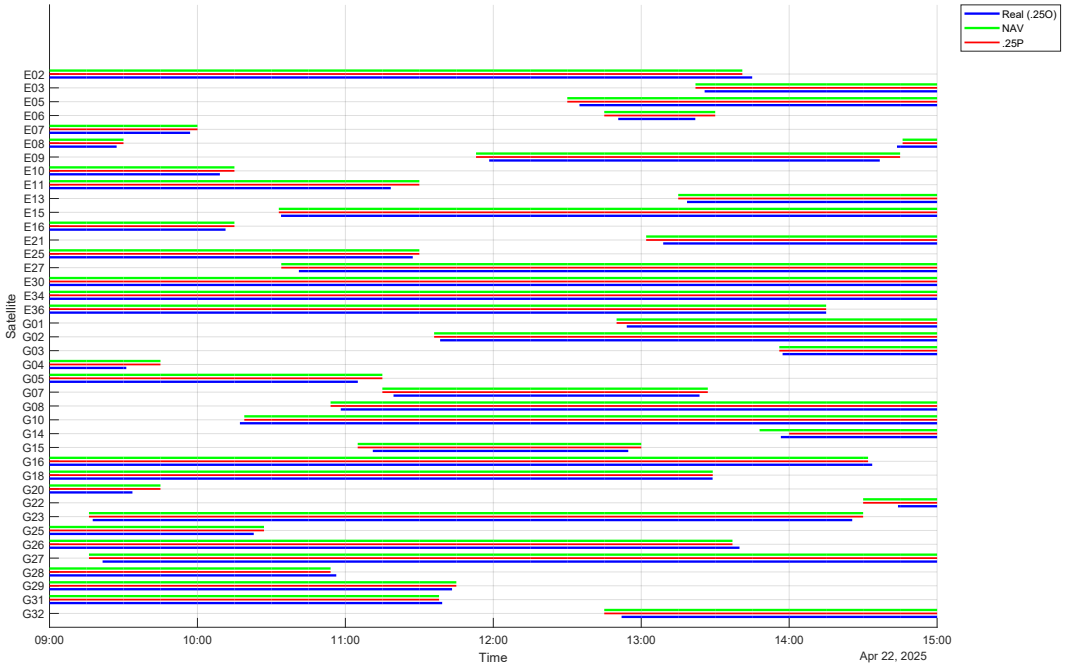

Figure 3.9: Comparison of satellite visibility intervals: real tracking (.25O), simulated NAV and receiver prediction (.25P).

are most apparent at the edges of the visibility windows, when a satellite is first acquired or lost by the receiver.

Both the NAV-based and .25P predictions tend to slightly overestimate the true visibility windows, often predicting satellite visibility to begin earlier or end later than what is actually observed. This behaviour may derive from different visibility mask assumptions: the simulator might use a lower elevation cut-off, while the receiver could apply stricter thresholds to determine whether a satellite is trackable.

In order to better quantify these timing discrepancies, a statistical analysis was performed on the start and end times of each visibility interval. Figure 3.10 summarizes the timing differences between the visibility times predicted using broadcast ephemerides (NAV) and those recorded in the real observations (.25O). For each satellite, the error in both acquisition time ($|\Delta\text{Start}|$) and loss time ($|\Delta\text{End}|$) is shown, expressed in absolute value.

The results indicate that the majority of satellites exhibit average timing errors below one minute, with many well under 30 seconds. This is further supported by the Cumulative Distribution Functions (CDFs) of the absolute start and end errors per satellite, shown in Figures 3.11a and 3.11b. From these plots, it can be observed that over 80% of satellites have acquisition and loss timing errors below 60 seconds, and over half fall below the 30-second threshold. These results confirm

that the simulation tool provides reliable predictions of visibility times in most cases.

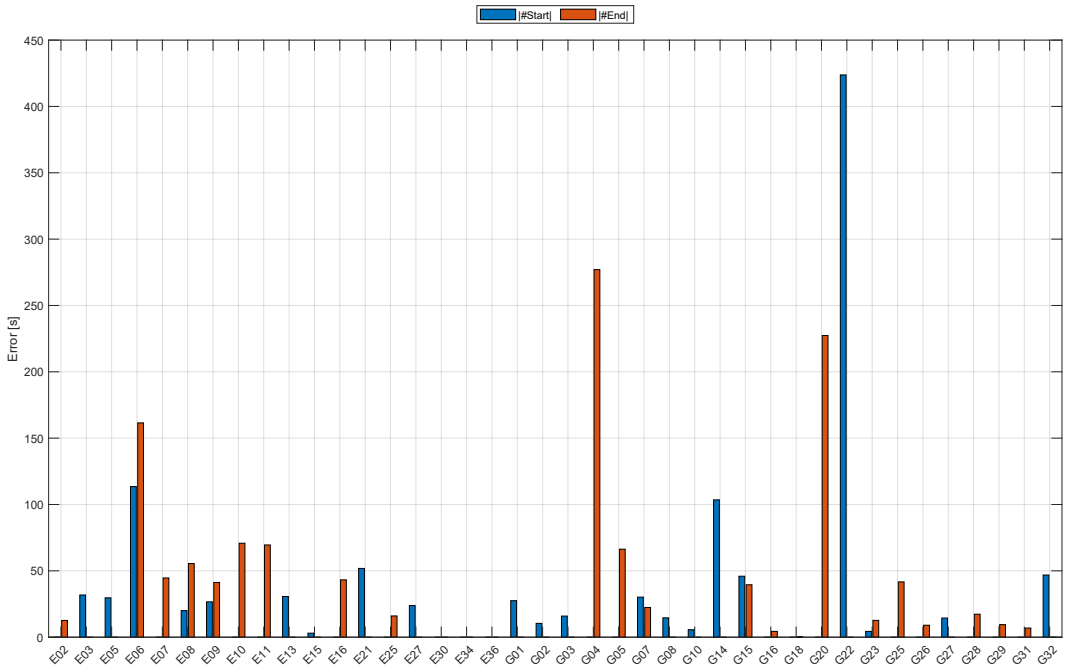

Figure 3.10: Visibility prediction errors per satellite: NAV-based predictions vs. real observations.

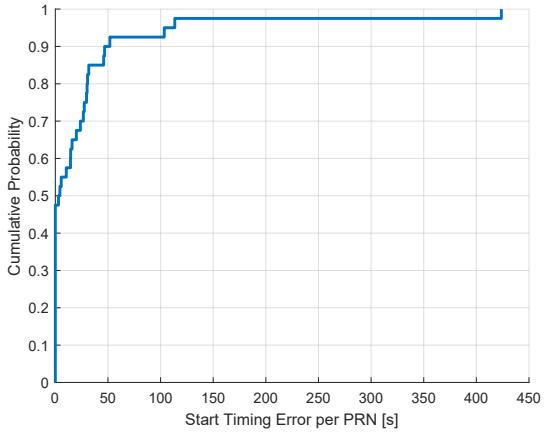

(a) CDF of $|\Delta\text{Start}|$ timing error per PRN (NAV).

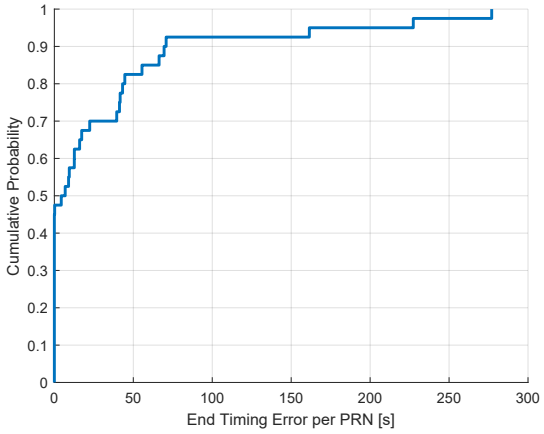

(b) CDF of $|\Delta\text{End}|$ timing error per PRN (NAV).

Figure 3.11: Cumulative distribution of timing errors per satellite, for acquisition and loss.

A few satellites exhibit slightly larger errors and also some clear outliers can be identified, such as `E06`, `G04`, `G14`, `G20` and `G22`, which exhibit more significant deviations in either acquisition or loss time.

These larger timing errors generally correspond to satellites observed at very low elevation angles during the initial or final moments of their visibility windows. This trend is quantitatively confirmed in Figure 3.12, which shows a clear correlation between high timing errors and low elevation angles. Satellites whose mean elevation falls below approximately 10° tend to exhibit significantly larger prediction errors.

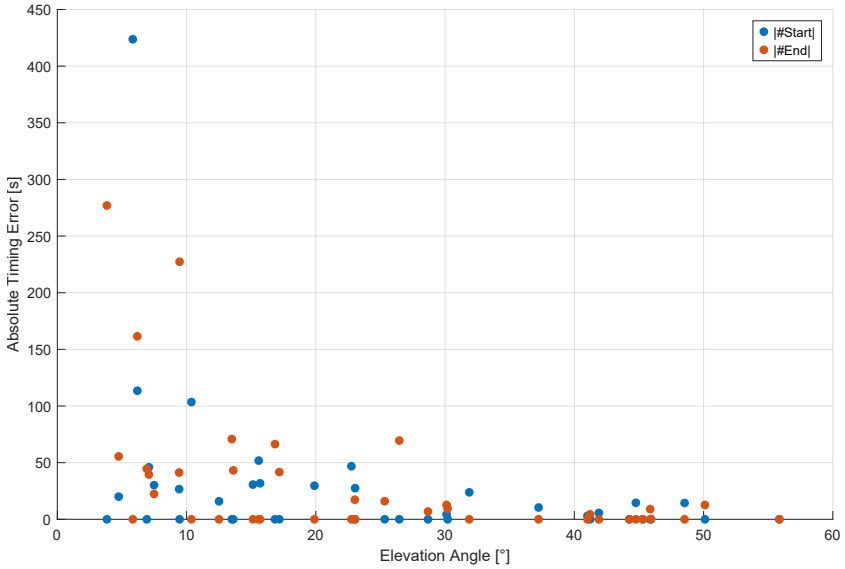

Figure 3.12: Timing error vs. Elevation angle at acquisition/loss per PRN (NAV).

As confirmed by the elevation plots (Figures 3.13a–3.13d), satellites such as `E06`, `G04`, `G14`, `G20` and `G22` exhibit brief visibility periods at low elevation, conditions in which accurate prediction is more challenging due to a combination of factors such as local obstructions, like buildings or terrain that can block the signal even if it is technically above the horizon, or small discrepancies in elevation mask thresholds between the simulator and the receiver which can significantly impact the exact acquisition or loss time. As a result, visibility predictions at low elevations are more prone to timing deviations.

A small subset of satellites, namely `E30`, `E34`, `E36` and `G18`, show zero timing error for both acquisition and loss. This occurs simply because these satellites were continuously visible throughout the entire observation window: since neither the real nor the predicted visibility windows had an identifiable start or end within this period, both sources naturally coincide.

The overall symmetry between acquisition and loss errors for most satellites indicates that the prediction algorithm performs consistently at both edges of

the visibility intervals. This confirms the suitability of the simulator as a reliable tool for visibility forecasting, particularly in the context of GNSS-based mission planning and performance analysis.

To provide a more global overview of the prediction accuracy, aggregated timing metrics were also computed across all satellites. On average, the NAV-based predictions show an acquisition time error of 13.10 s (standard deviation 71.35 s) and a loss time error of 14.62 s (standard deviation 81.38 s), leading to a mean duration error of 27.72 s. The .25P-based predictions perform similarly, with mean acquisition and loss time errors of 12.00 and 14.65 s, respectively, and a duration error of 26.65 s.

In both cases, the predicted visibility intervals match the real observations extremely well, with an average temporal overlap of 99.66% across all satellites. These values confirm the overall consistency and reliability of the predictions.

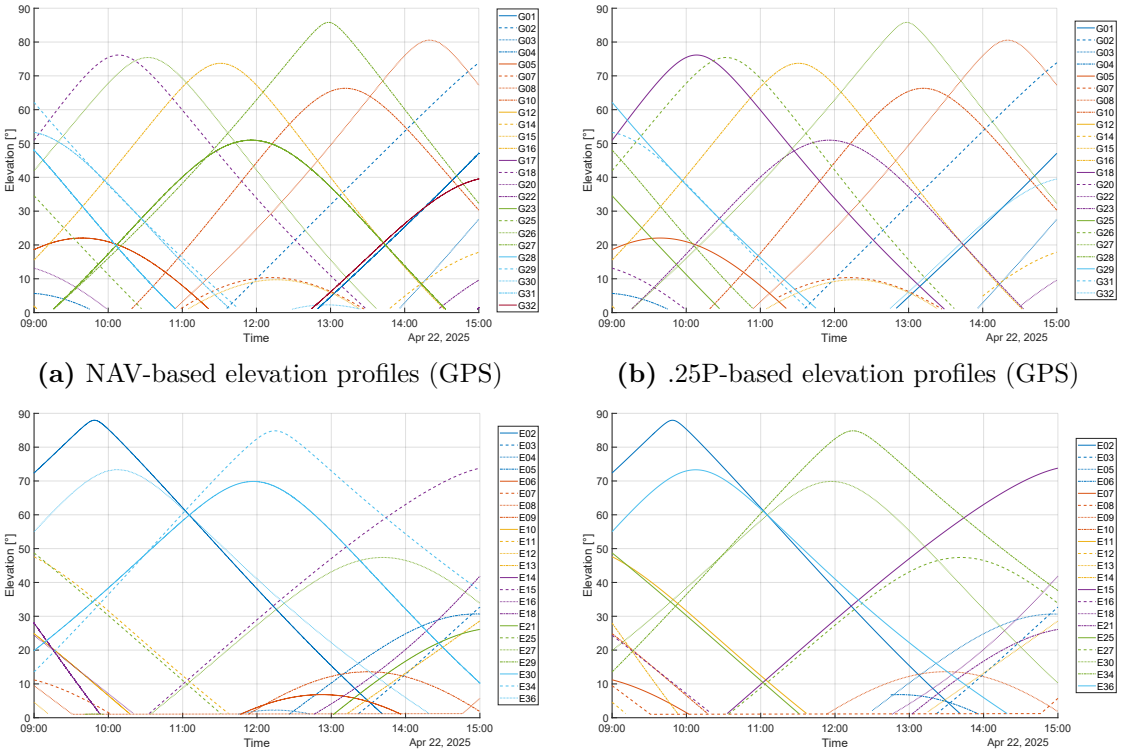

(a) NAV-based elevation profiles (GPS)

(b) .25P-based elevation profiles (GPS)

(c) NAV-based elevation profiles (Galileo)

(d) .25P-based elevation profiles (Galileo)

Figure 3.13: Elevation angles of all tracked satellites over the test window, divided by constellation (GPS/Galileo) and prediction source (NAV/.25P).

Finally, it is important to mention that four satellites, `E04`, `E29`, `G17` and `G30`, appear in the NAV-based predictions but were not detected in the actual observations or in the .25P data. These cases represent false positives in the

simulation output and may be due to visibility events occurring at very low elevation angles, filtered out by the receiver's tracking algorithms. Although rare, such discrepancies highlight the need to carefully account for visibility constraints (e.g., elevation masks) when interpreting prediction results. Despite this, the simulator demonstrates a high level of correlation with real-world data for the vast majority of cases.

To further explore the impact of low-elevation tracking on the accuracy of visibility predictions, an additional validation was performed by applying an elevation mask of 6° to the simulation process. Under this updated constraint, visibility events occurring below 6° were removed from both the simulation and comparison process. As a result, certain short or marginal visibility intervals, particularly those associated with extreme errors in the previous analysis, were excluded.

The updated metrics obtained with this constraint are:

- NAV-based predictions show a mean acquisition error of 14.39 s (standard deviation 77.43 s) and a mean loss error of 18.65 s (standard deviation 96.21 s), resulting in an overall duration error of 33.04 s.
- .25P-based predictions yield identical values, with a mean acquisition error of 14.39 s and an overall duration error of 33.04 s.
- The average temporal overlap between simulated and observed visibility intervals slightly decreased to 96.10%, compared to 99.66% in the baseline case.

These results highlight the trade-off introduced by the elevation mask: on one hand, the slight reduction in overlap and marginal increase in average timing errors indicate a more conservative visibility estimation, as borderline segments are ignored. On the other hand, the removal of low-elevation events leads to an increased level of robustness: the most extreme outliers observed previously, errors exceeding 400 s, are no longer present.

This improvement is clearly visible in the updated bar and scatter plots (Figures 3.15 and 3.17), where no satellite exhibits errors beyond 180 seconds. The cumulative distribution functions in Figures 3.16a and 3.16b further reinforce this observation, showing that more than 90% of the satellites now have acquisition and loss errors below 100 s.

The updated scatter plot in Figure 3.17 shows a clearer relationship between the timing error and the elevation angle. Unlike the previous case, where the largest errors were concentrated below a 10° threshold and the above values seemed to be on the same line, the filtered dataset spreads more evenly across the 6°–20° range. Nevertheless, higher elevation angles, above roughly 20°, consistently correspond to low timing errors, reinforcing the observation that prediction uncertainty is most pronounced near the visibility boundary.

The elevation profiles for all satellites remain identical to those shown previously, except for the absence of segments below 6°, which were filtered out by the new mask.

Overall, an elevation mask of 6° can be considered an optimal trade-off configuration. Despite resulting in a slightly lower overlap compared to the baseline case, it provides significantly improved robustness by suppressing extreme outliers. In particular, it achieves the lowest range of acquisition and loss errors among all tested configurations.

Tests with a lower elevation threshold (e.g., 2° or 3°) resulted in higher overlap values, but also reintroduced large timing deviations, as marginal visibility events remained in the analysis and produced long simulated intervals not matched by real tracking. On the other hand, applying stricter masks (e.g., 7° or higher) reduced the overlap further and introduced timing errors in the opposite direction, as the predicted visibility intervals became shorter than the observed ones. These results confirm that a 6° elevation mask provides the best balance between prediction accuracy and temporal coverage.

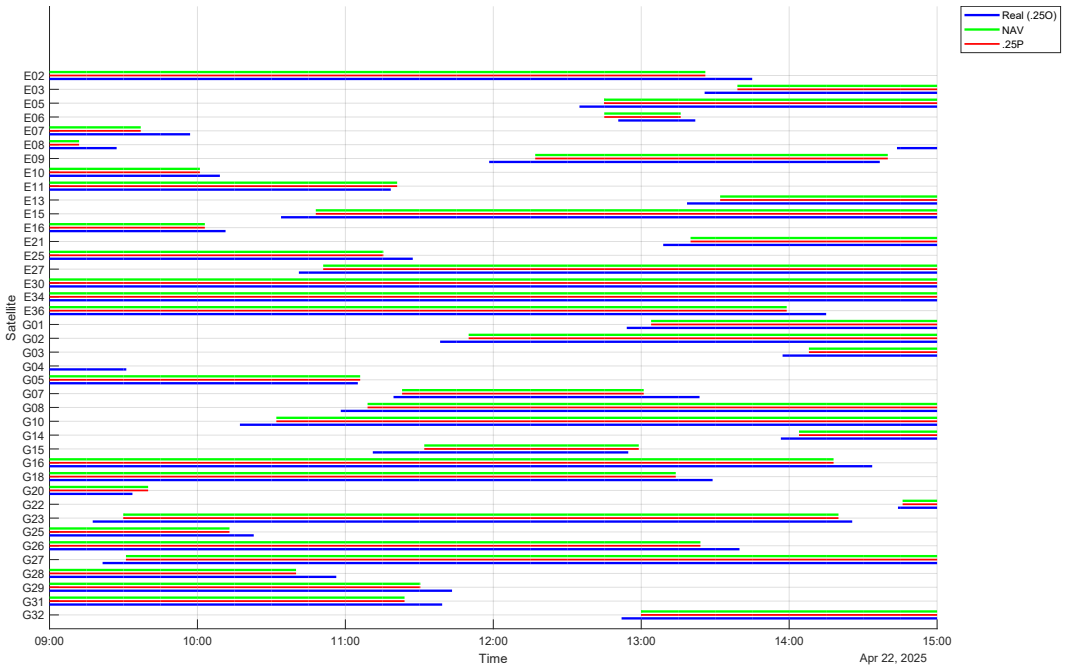

Figure 3.14: Comparison of satellite visibility intervals with elevation mask at 6°: real tracking (.25O), simulated (NAV) and receiver prediction (.25P).

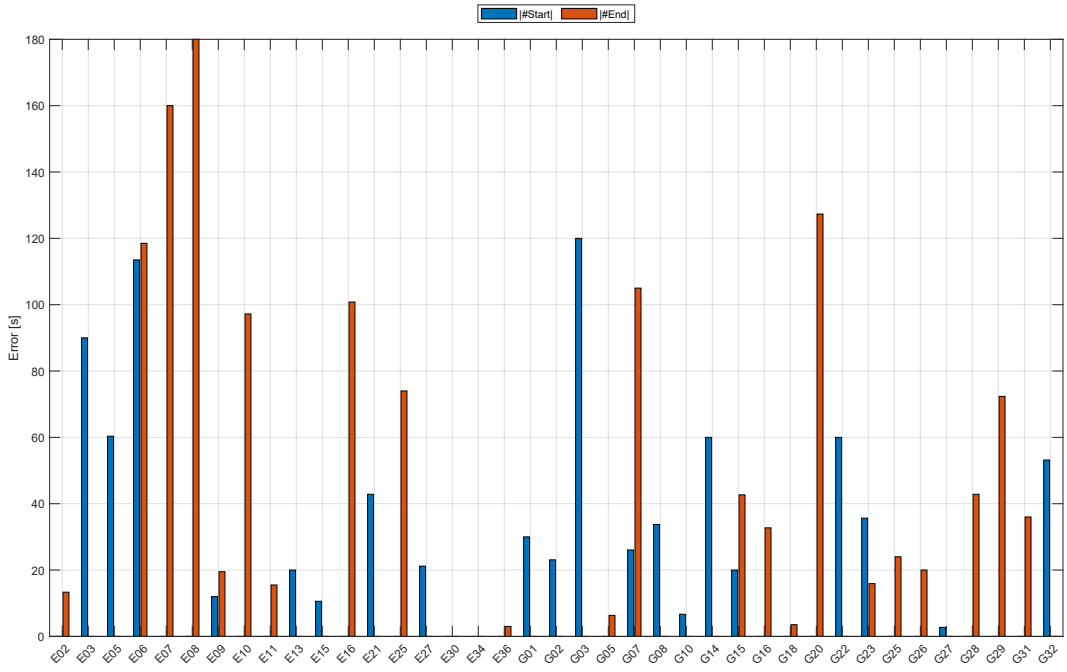

Figure 3.15: Visibility prediction errors per satellite after applying a 6° elevation mask.

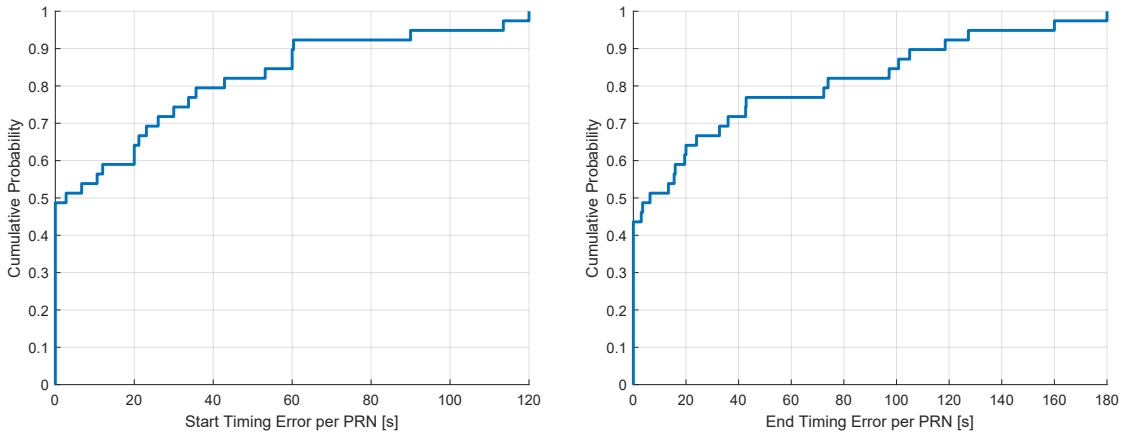

(a) CDF of $|\Delta\text{Start}|$ **(b)** CDF of $|\Delta\text{End}|$

Figure 3.16: Cumulative distribution of timing errors with elevation $> 6°$.

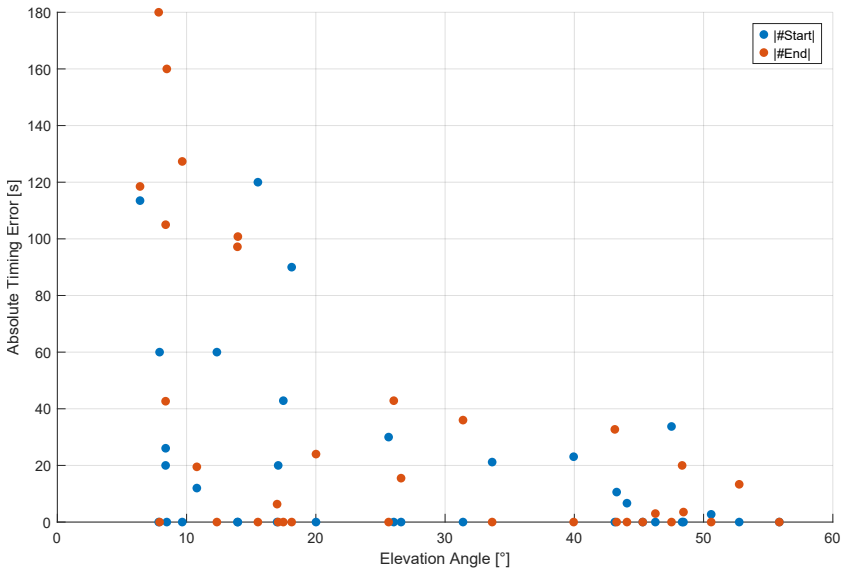

Figure 3.17: Timing error vs. elevation angle at acquisition/loss with 6° elevation mask.

Although obtained under terrestrial conditions, these validation results show that the visibility planner behaves consistently with real multi-constellation observations and can therefore be used with confidence in the cislunar simulations presented in the next section.

3.4 Cislunar Navigation Scenarios

After validating the behaviour of the simulator under terrestrial conditions, the framework was used to address the main goal of this work: evaluating the performance and limitations of GNSS-based navigation in the cislunar region and examining how a lunar beacon could improve the overall geometry. In order to do this, a set of representative scenarios was defined. These scenarios were designed to test different geometric and radiometric configurations, exploring both simple, ideal cases and more realistic setups that might reflect practical mission constraints.

The lunar beacon, whose model was introduced in Section 3.2.2, plays an important role in all the scenarios. Depending on its antenna pointing strategy, either fixed toward Earth or dynamically tracking the spacecraft, the scenarios allow for the analysis of how signal availability, link quality and geometric coverage vary under different operating conditions and so, for the characterization of a potential augmentation element.

The receiver's antenna orientation was also varied across scenarios, with configurations either constantly directed toward Earth or dynamically tracking the

lunar beacon. The combination of transmitter and receiver pointing strategies allowed the evaluation of multiple navigation scenarios with distinct geometric and radiometric characteristics, enabling the identification of the configuration that offer the most favourable navigation performance in the cislunar environment.

The following sections provide a detailed description of the three selected scenarios.

3.4.1 Scenario 1: Mutual Pointing

This first scenario represents a fully cooperative configuration in which both the transmitter (the lunar beacon) and the receiver (the spacecraft) dynamically orient their antennas toward each other. The beacon actively tracks the spacecraft's position and continuously points its main lobe to maintain maximum gain along the line of sight. At the same time, the spacecraft is equipped with a dedicated antenna capable of real-time tracking of the beacon, ensuring optimal reception of the transmitted signal.

Such mutual pointing ensures optimal geometric and radiometric conditions throughout the entire trajectory. By maintaining a stable line of sight and minimizing the angular deviation from the antenna main lobes, the configuration enables maximal C/N_0. Since both ends of the communication link operate under idealized gain and alignment conditions, this scenario provides a theoretical upper bound for signal strength, link availability and overall navigation performance in a cislunar context.

The geometry of this mutual-pointing scenario is illustrated in Figure 3.18, which shows the relative positions of the spacecraft and the Moon over the simulated period. The blue vectors represent the pointing direction of the beacon as it continuously tracks the spacecraft, while the green vectors indicate the pointing direction of the spacecraft's antenna toward the beacon. The labeled epochs provide reference points along the trajectory to visualize the consistency of the mutual alignment throughout the 2000 simulated epochs, corresponding to approximately 33 hours of mission time.

3.4.2 Scenario 2: Beacon Fixed Toward Earth

The second scenario explores a simplified and operationally conservative configuration in which the lunar beacon continuously transmits GNSS-like signals toward Earth, with a fixed antenna pointing direction toward the centre of the Earth. This setup reflects the assumption of a passive beacon designed to provide service to Earth-based or Earth-orbiting users, without active tracking capabilities. On the spacecraft side, the GNSS antenna is also designed to have a fixed orientation, constantly aligned with the Earth-centered reference frame, similar to the design

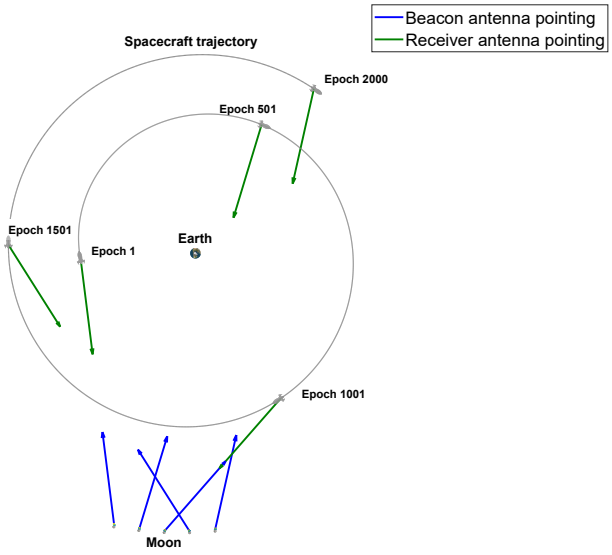

Figure 3.18: Scenario 1: the beacon and the spacecraft track each other throughout the trajectory.

adopted for the LuGRE mission [35].

In this configuration, the beacon does not require any attitude control, as it is fixed on the lunar surface and permanently oriented toward the Earth. The receiver, on the other hand, must still maintain its Earth-pointing orientation while moving along the trajectory, so only the beacon operates in a fully passive mode. This setup also introduces geometric constraints that depend on the relative motion of the Earth, Moon and spacecraft. As the geometry evolves, the alignment between the beacon's antenna and the spacecraft can degrade, reducing the available gain and potentially leading to periods in which the spacecraft moves outside the beacon's main lobe.

From a radiometric point of view, this scenario tends to result in lower and more variable received C/N_0 compared to the mutual pointing case. Still, it represents a more realistic baseline for evaluating navigation feasibility under minimalistic assumptions and passive hardware. The results provide insight into the extent and quality of coverage achievable with an Earth-focused beacon and a non-tracking spacecraft receiver operating in the cislunar environment.

A graphical representation of this scenario is provided in Figure 3.19, illustrating the fixed antenna orientations of both the beacon and the spacecraft toward Earth.

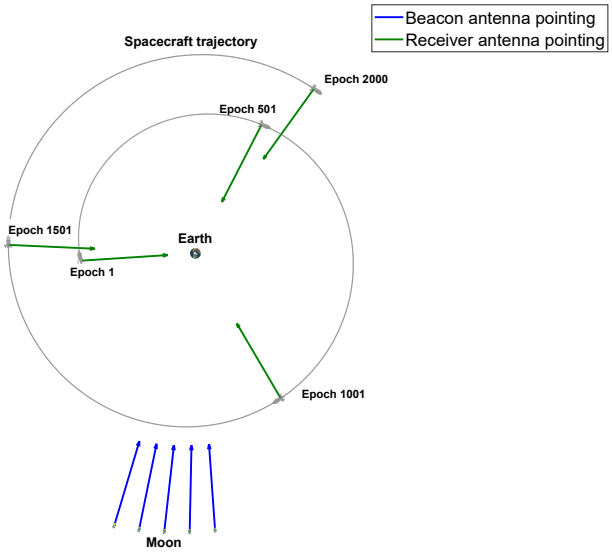

Figure 3.19: Scenario 2: the lunar beacon and the spacecraft's antenna are both pointing towards the centre of the Earth.

3.4.3 Scenario 3: Fixed Beacon Pointing to Earth and Receiver Tracking the Beacon

The third scenario considers a semi-cooperative configuration where the lunar beacon transmits GNSS-like signals using a fixed antenna pointing toward Earth, like in the second scenario, while the spacecraft is equipped with a dedicated antenna that actively tracks the beacon throughout the mission, as in the first scenario analyzed.

The fixed Earth-pointing beacon replicates a passive deployment strategy, minimizing complexity, power requirements and control logic on the lunar surface. However, by enabling the spacecraft to dynamically point its antenna toward the beacon, the link benefits from improved alignment and received signal strength compared to the previous scenario.

To avoid a geometric conflict between the direction of the beacon and the field of view required for GNSS reception, this scenario assumes that the spacecraft carries two separate antennas. The GNSS antenna must remain Earth-aligned in order to keep all GNSS satellites within its narrow field of view, whereas the beacon link requires a different pointing direction that varies along the trajectory. Using a single antenna would therefore force the spacecraft to choose between maintaining GNSS visibility or tracking the beacon. By separating the two functions, a fixed Earth-pointing GNSS antenna and a steerable high-gain antenna dedicated to the beacon, the spacecraft can track the beacon without degrading GNSS reception.

This configuration provides a performance trade-off: the fixed pattern of the beacon can result in non-optimal transmission to the spacecraft depending on its relative position, but the adaptive pointing of the receiver helps to preserve beneficial values of C/N_0 for most of the trajectory. The result is an intermediate level of link robustness and signal availability between the two previous scenarios.

This hybrid approach is relevant for future mission designs trying to balance operational simplicity with enhanced radiometric performance. A graphical overview of the scenario, showing the fixed Earth-directed transmission beam and the spacecraft's active tracking antenna, is presented in Figure 3.20.

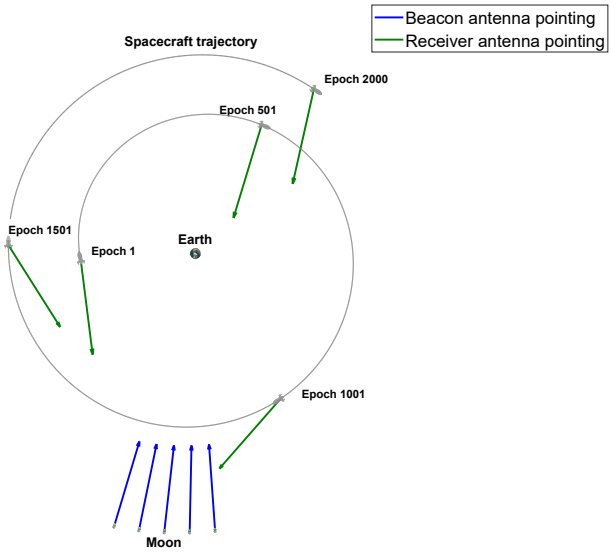

Figure 3.20: Scenario 3: the lunar beacon is fixed toward Earth, while the spacecraft dynamically tracks the beacon.

Chapter 4

Results

This chapter presents the results of the simulation campaign performed on the three cislunar scenarios defined in Section 3.4. For each scenario, the analysis focuses on the behaviour of the received signals along the reference trajectory, examining the resulting C/N_0 levels under different beacon pointing configurations.

A final section provides a consolidated comparison between the cases with and without the lunar beacon, highlighting its impact on the quality of the navigation solution and on the achievable positioning accuracy along the trajectory.

4.1 Analysis of Cislunar Scenarios

This section presents the performance results obtained for each of the simulated cislunar scenarios. The goal is to assess how different transmitter and receiver pointing strategies affect key navigation metrics such as C/N_0 and antenna alignment. The analysis is based on the same mission trajectory and timing setup for all scenarios, ensuring a consistent basis for comparison.

4.1.1 Scenario 1: Beacon Tracking the Spacecraft

In the first simulated scenario both the lunar beacon (transmitter) and the spacecraft (receiver) maintain continuous reciprocal pointing. At each epoch, the beacon dynamically steers its antenna toward the spacecraft, and the spacecraft's antenna reciprocally aligns with the beacon. As a result, both antennas operate at maximum gain along the line of sight for the entire duration of the simulation.

The received C/N_0 is computed through the standard link budget equation:

$$C/N_0 = P_{\text{tx}} + G_{\text{tx}} + G_{\text{rx}} - L_{\text{fs}} - L_{\text{pol}} - R_{\text{loss}} - 10\log_{10}(k_B T_{\text{sys}}) \tag{4.1}$$

where:

- $P_{\text{tx}} = 16$ dBW is the transmitter output power;
- G_{tx} and G_{rx} are the transmitter and receiver antenna gains, respectively;
- L_{fs} is the free-space path loss, expressed as:

$$L_{\text{fs}} = 20 \log_{10} \left(\frac{4\pi d}{\lambda} \right) \tag{4.2}$$

  where d is the instantaneous beacon–spacecraft distance and λ is the signal wavelength;
- $\lambda = \frac{c}{f}$, where $c = 2.9979 \times 10^8$ m/s is the speed of light and $f = 1.57542$ GHz is the carrier frequency, corresponding to the L1 frequency band;
- $L_{\text{pol}} = 1$ dB represents the polarization mismatch loss;
- $R_{\text{loss}} = 0.9$ dB accounts for receiver front-end losses;
- $k_B = 1.380649 \times 10^{-23}$ J/K is the Boltzmann constant;
- $T_{\text{sys}} = 162$ K is the system noise temperature.

The numerical values adopted in the link-budget model follow the same configuration used in the original simulation tool on which this work is based. That tool already included a reference GNSS receiver and transmitter setup designed for deep-space applications, and the parameters implemented there were selected to represent realistic operating conditions without introducing unnecessary assumptions. For this reason, the same values were retained here, ensuring continuity with the validated baseline.

The antenna gains G_{tx} and G_{rx} are derived from the corresponding radiation patterns. In this ideal configuration, due to almost perfect reciprocal pointing, the gains are fixed to the maximum value of each pattern for the entire simulation. This assumption is verified by monitoring the angle between each antenna's boresight and the LOS vector, defined as:

$$\theta = \cos^{-1} \left(\hat{\mathbf{u}}_{\text{boresight}} \cdot \hat{\mathbf{u}}_{\text{LOS}} \right) \tag{4.3}$$

where $\hat{\mathbf{u}}_{\text{boresight}}$ and $\hat{\mathbf{u}}_{\text{LOS}}$ are normalized vectors. The normalization ensures that θ measures the pure directional misalignment, independent of the vector magnitudes.

Figure 4.3 shows the evolution in time of both angles. In this ideal configuration, the two curves are practically indistinguishable, with values remaining on the order of 10^{-6} degrees for the entire simulation. The small deviations from zero are only due to numerical precision effects, confirming the assumption of perfect reciprocal

pointing and justifying the use of constant maximum antenna gains for both ends of the link.

The temporal evolution of C/N_0 is shown in Figure 4.1. The maximum value, roughly 52.5 dB-Hz, is reached around epoch 1150, with variations between 41 and 52.5 dB-Hz over the scenario. Figure 4.2 displays the corresponding distance profile, highlighting an inverse correlation between C/N_0 and distance. This is consistent with the logarithmic dependency of the free-space path loss on distance:

$$L_{\text{fs}} \propto 20 \log_{10}(d) \tag{4.4}$$

where L_{fs} is expressed in dB.

A shorter distance reduces the path loss, increasing the received power and thus C/N_0. The minimum distance occurs near epoch 1150, coinciding with the C/N_0 peak, confirming the expected physical relationship.

This behaviour is consistent with the geometry of the scenario shown in Figure 3.18, where the spacecraft approaches the lunar surface around epoch 1150.

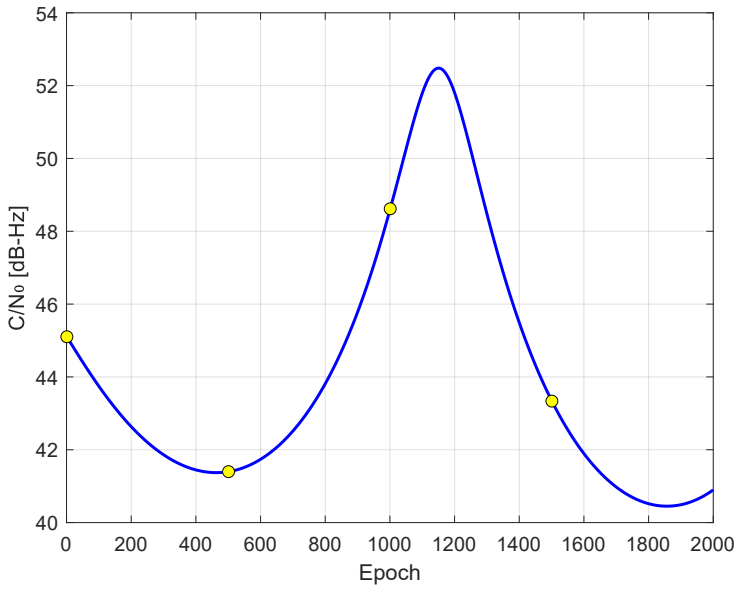

Figure 4.1: Received C/N_0 over time in the mutual-pointing scenario.

In addition to the forward link budget analysis used to estimate the received C/N_0, an inverse link budget evaluation was performed to determine the maximum transmit power $P_{\text{tx,max}}$ that the lunar beacon could radiate without exceeding the interference protection threshold defined for GPS L1 signals at the Earth's surface. According to the GPS Interface Specification IS-GPS-200N [36, Table 3-Va], the minimum received RF signal strength for the L1 service is $P_{\text{rx,limit}} = -158.5\,\text{dBW}$.

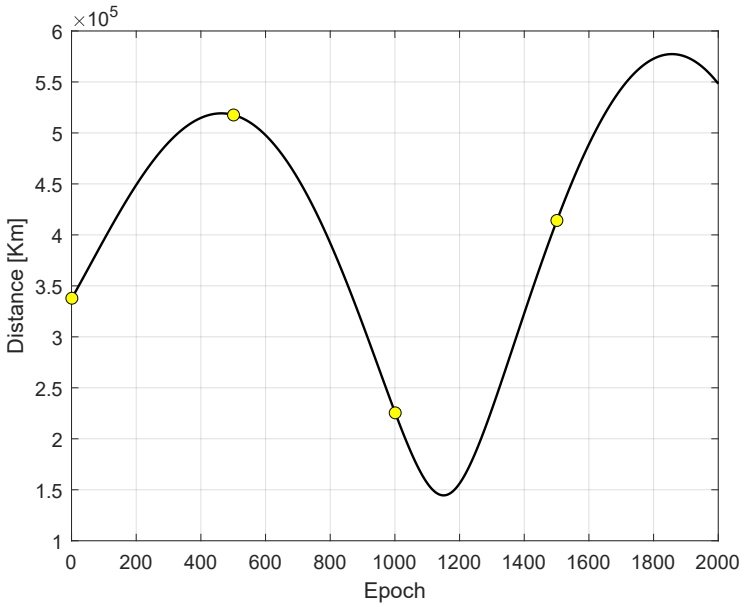

Figure 4.2: Distance between the spacecraft and the lunar beacon.

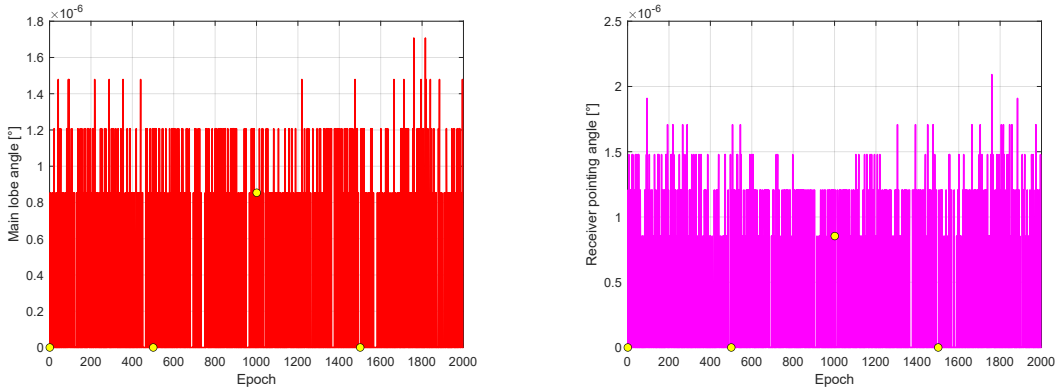

(a) Beacon boresight vs LOS

(b) Receiver boresight vs LOS

Figure 4.3: Alignment angles with respect to the line-of-sight.

This value was adopted as the maximum allowable received power at a reference user antenna located at the point on Earth directly facing the Moon.

At each simulation epoch, the maximum admitted transmit power was computed as:

$$P_{\text{tx,max}} = P_{\text{rx,limit}} + L_{\text{fs}} - G_{\text{tx}\rightarrow\text{Earth}} - G_{\text{rx,ref}} \tag{4.5}$$

where:

- L_{fs} is the free-space path loss from the beacon to the Earth point.
- $G_{\mathrm{tx}\to\mathrm{Earth}}$ is the beacon antenna gain in the direction of the Earth,
- $G_{\mathrm{rx,ref}} = 3\,\mathrm{dBi}$ is the gain of the reference user antenna, consistent with the reference user antenna gain defined in the GPS Interface Specification IS-GPS-200N [36, Sec. 3.3.1.6], which specifies this value for a linearly polarized ground-based antenna in nominal orientation.

The most restrictive condition occurred at epoch 1177, as illustrated in Figure 4.4. In this geometry, the beacon's antenna gain toward Earth was 15.34 dBi, the free-space path loss reached 207.90 dB and the Earth–beacon distance was approximately 376 189 km. By substituting these values into (4.5), the resulting worst-case maximum allowed transmit power is 31.06 dBW, beyond which the beacon would exceed the GPS L1 interference threshold at the Earth's surface.

The temporal evolution of the Earth–beacon distance during the simulation is reported in Figure 4.5. As expected, this distance remains nearly constant throughout the scenario because the beacon is fixed on the lunar surface and the Earth–Moon separation varies only slightly over the considered time frame. This same distance profile also applies to Scenarios 2 and 3, since the beacon's location on the Moon is unchanged.

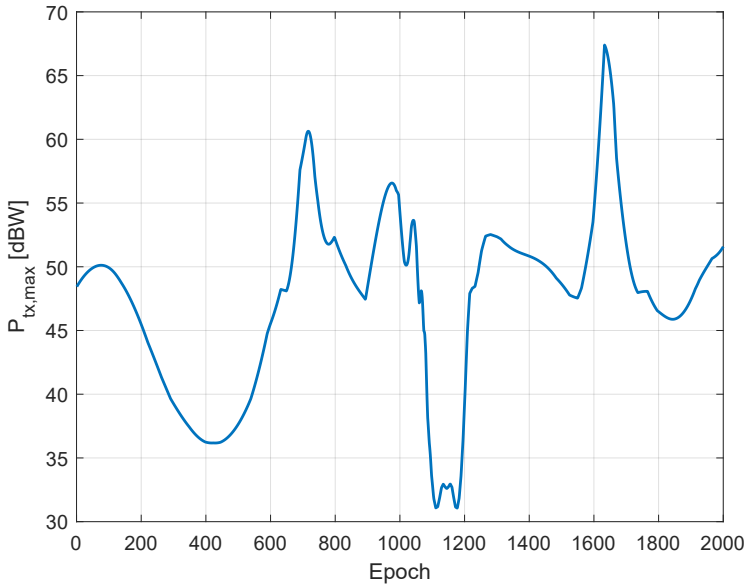

Figure 4.4: Maximum allowed beacon transmit power $P_{\mathrm{tx,max}}$ over time in Scenario 1.

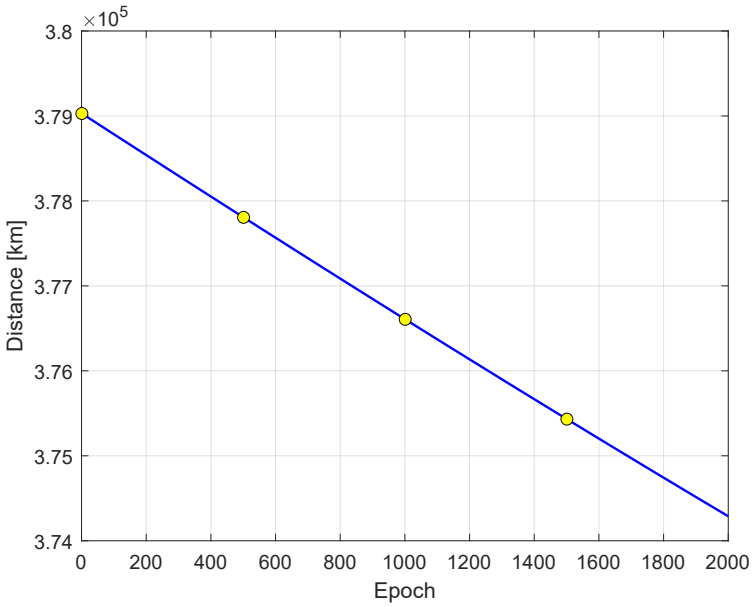

Figure 4.5: Distance between the Earth and the lunar beacon over the simulation period.

4.1.2 Scenario 2: Beacon Fixed Toward Earth

The second simulated scenario corresponds to the dual Earth-pointing geometry introduced in Section 3.4.2, where both the lunar beacon and the spacecraft keep their antennas fixed toward the Earth's center. In this configuration the beacon operates in a fully passive mode, while the spacecraft antenna must maintain its Earth-pointing orientation while moving along the trajectory, so the pointing is not completely passive on both sides.

The fixed pointing geometry implies that the instantaneous alignment between each antenna boresight and the beacon–spacecraft LOS varies significantly over time, depending on the relative positions of the Earth, Moon and spacecraft. The beacon and receiver alignment angles are computed as in (4.3), with $\hat{\mathbf{u}}_{\text{boresight}}$ and $\hat{\mathbf{u}}_{\text{LOS}}$ denoting the normalized boresight and LOS vectors, respectively. Figure 4.7 shows their temporal evolution. Unlike in the mutual-pointing case, the angles exhibit large variations, with values exceeding 100° for the receiver in certain epochs, indicating severe misalignment between antennas.

The corresponding C/N_0 profile, reported in Figure 4.6, reflects the combined influence of antenna pointing and distance. Compared to the ideal reciprocal point case (Figure 4.1), C/N_0 is overall lower and more variable, with peaks around 17 dB-Hz and frequent drops below 0 dB-Hz. The distance profile remains identical to Scenario 1 (Figure 4.2), as the spacecraft trajectory is unchanged.

An interesting feature occurs around epoch 1150: despite the receiver pointing angle approaching 180°, C/N_0 exhibits a local maximum. This counter-intuitive behaviour is explained by the concurrent minimum in beacon–spacecraft distance, which drastically reduces the free-space path loss L_{fs} according to Eq. (4.2). The gain loss due to antenna misalignment is thus partially compensated by the shorter propagation path, preventing C/N_0 from reaching its lowest values. This highlights the dominant role of distance in the link budget when the antenna pattern does not drop sharply in that direction.

Overall, this scenario shows how sensitive the link quality becomes under passive dual Earth-pointing. Depending on the geometry, short intervals of improved C/N_0 may occur due to proximity, but the general performance remains well below that achieved with active mutual pointing.

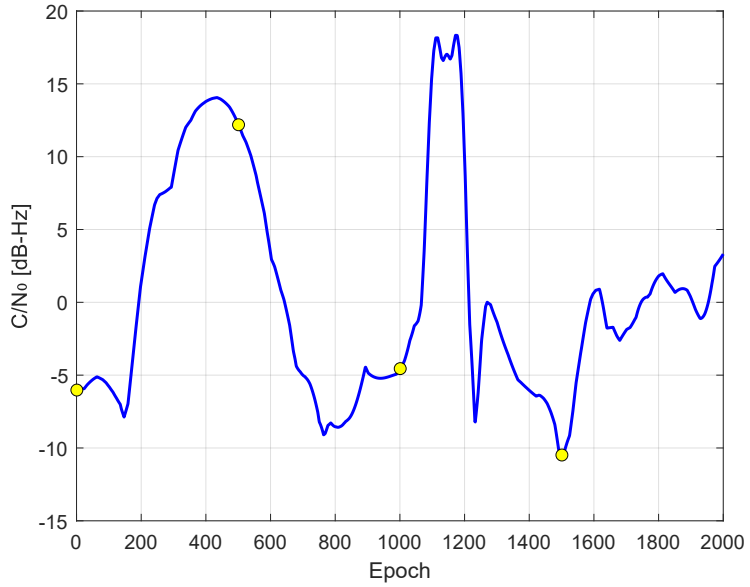

Figure 4.6: Received C/N_0 over time in the dual Earth-pointing scenario.

For this scenario, the most restrictive condition occurred at epoch 2000, as illustrated in Figure 4.8. At that epoch, the beacon's antenna gain toward Earth was 13.85 dBi, the free-space path loss reached 207.86 dB and the Earth–beacon distance was approximately 374 288 km. Substituting these values into the inverse link budget equation gives a worst-case maximum allowed transmit power of 32.51 dBW, above which the beacon would exceed the GPS L1 interference protection threshold at the Earth's surface.

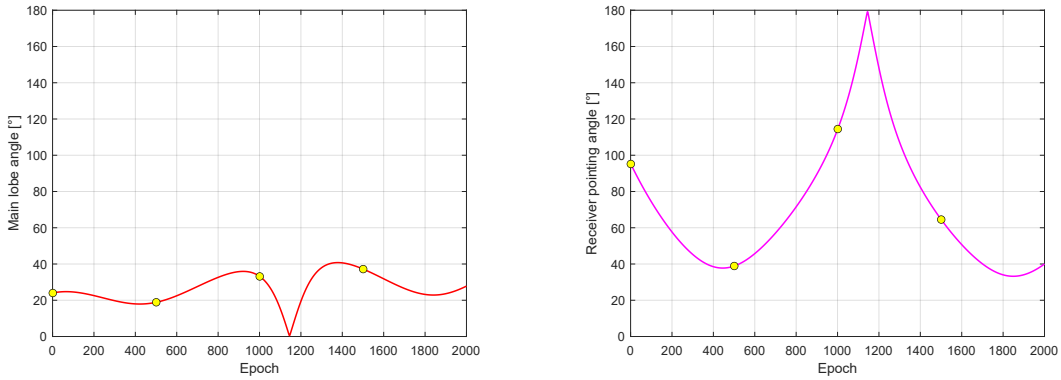

(a) Beacon boresight vs LOS

(b) Receiver boresight vs LOS

Figure 4.7: Alignment angles for the beacon (a) and the receiver (b) in the dual Earth-pointing scenario.

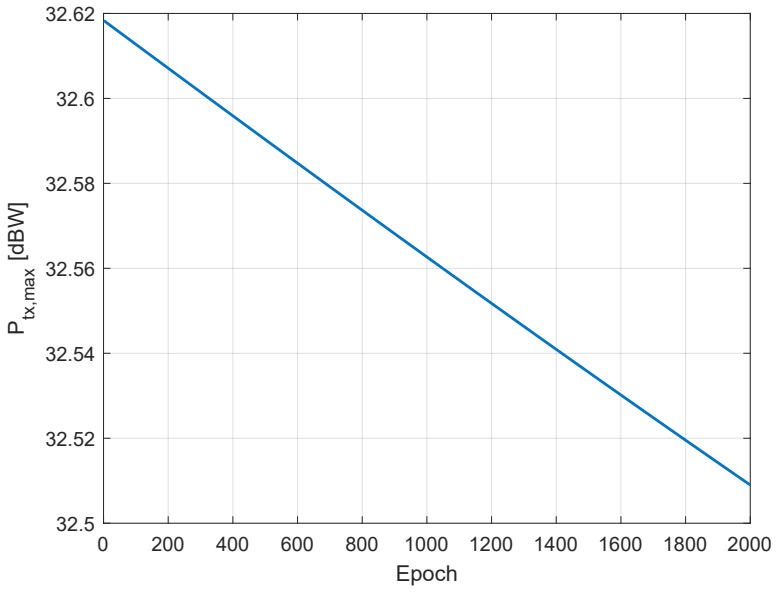

Figure 4.8: Maximum allowed beacon transmit power $P_{\text{tx,max}}$ over time in Scenario 2.

4.1.3 Scenario 3: Beacon and Dedicated RX Antenna

In this configuration, the lunar beacon maintains a fixed pointing toward the Earth's centre, replicating the passive transmission strategy of Scenario 4.1.2. The difference lies on the receiver side: the spacecraft is equipped with an active

antenna tracking system that continuously aligns its boresight with the beacon. This hybrid architecture aims to combine the simplicity of a fixed transmitter with the performance benefits of dynamic pointing at the receiver side.

The received C/N_0 is computed as in Eq. (4.1), with the antenna gains G_{tx} and G_{rx} now evolving differently over time: G_{tx} depends on the beacon's fixed Earth-pointing pattern and the instantaneous angular offset with respect to the spacecraft, while G_{rx} remains fixed at its maximum value thanks to perfect tracking.

Figure 4.9 shows the C/N_0 evolution over the entire simulation. Compared to Scenario 4.1.2, the curve is significantly stronger and more stable: peaks exceed 50 dB-Hz around epoch 1150, while minimum values remain above 20 dB-Hz for most of the trajectory. The enhancement is attributed to the receiver's active pointing, which removes the geometric losses associated with a fixed spacecraft antenna.

The alignment performance is illustrated in Figure 4.10. The beacon's pointing angle (Figure 4.10a) replicates the profile of Scenario 4.1.2, varying between $\approx 0°$ and $\approx 40°$ as the spacecraft moves along its trajectory. In contrast, the receiver's pointing angle (Figure 4.10b) stays at the level of numerical noise ($\approx 10^{-6}°$), confirming that the tracking system maintains perfect alignment with the beacon throughout the simulation.

As in the previous scenarios, C/N_0 variations can be linked to the combined effect of distance and pointing geometry. Around epoch 1150, the spacecraft reaches its closest approach to the Moon, minimizing d and simultaneously benefiting from a small beacon pointing angle, which places the receiver well within the beacon's main lobe. This combination of favourable geometry and minimal path loss produces the C/N_0 peak observed in Figure 4.9.

Overall, this scenario demonstrates that even with a non-tracking, fixed Earth-pointing beacon, the use of active tracking at the receiver side preserves a strong and stable link budget. This makes the configuration an appealing trade-off for missions seeking to reduce complexity and resource demands at the transmitter while still achieving robust radiometric performance.

The inverse link budget analysis yields identical results to those obtained in Scenario 4.1.2. This happens because, in both configurations, the beacon's antenna maintains a fixed pointing toward the Earth, resulting in the same geometry with respect to the sub-Earth point and thus identical values of $G_{\text{tx}\to\text{Earth}}$, L_{fs}, and Earth–beacon distance at each epoch. Consequently, the maximum transmit power allowed in the worst case remains 32.51 dBW, as shown in Figure 4.8.

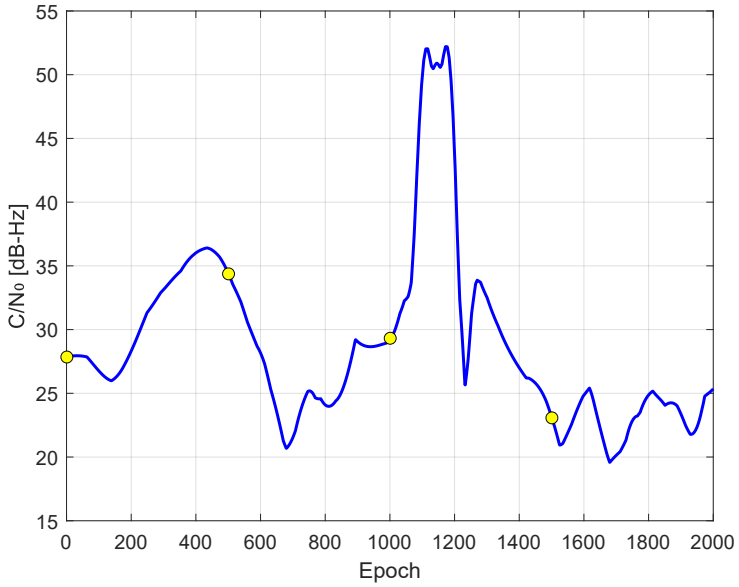

Figure 4.9: Received C/N_0 over time in Scenario 4.1.3.

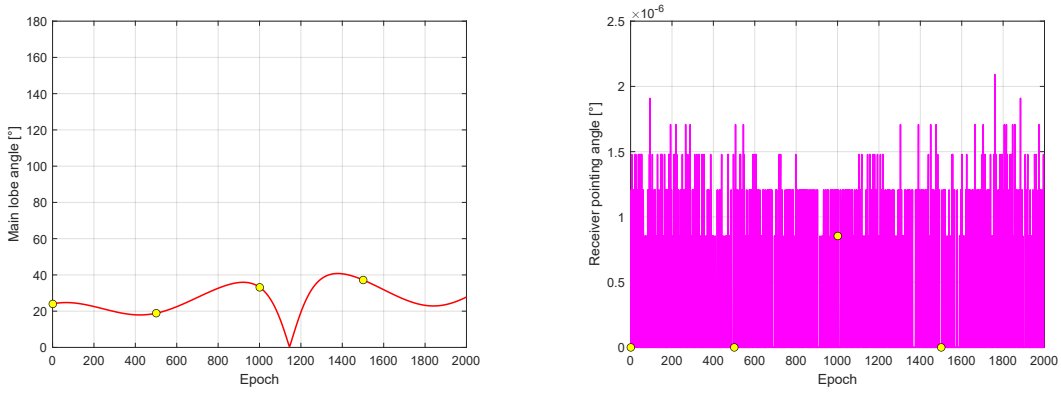

(a) Beacon boresight vs LOS

(b) Receiver boresight vs LOS

Figure 4.10: Alignment angles for the beacon (a) and the receiver (b) in Scenario 4.1.3.

4.2 Comparative Assessment and Discussion

The three simulated scenarios provide a clear picture of how different combinations of transmitter and receiver pointing strategies impact the quality and robustness of a cislunar navigation link. Rather than analyzing them individually, this section focuses on their relative performance, highlighting the main trade-offs between link

budget, temporal stability and operational complexity.

Table 4.1 summarizes the main quantitative indicators derived from the simulations. For each scenario, the maximum and minimum values of C/N_0 observed are reported, together with the corresponding peak-to-peak variation, defined as $\Delta_{\text{pp}} = (C/N_0)_{\max} - (C/N_0)_{\min}$. Operational complexity is qualitatively classified as *High*, *Medium* or *Low*, depending on the level of real-time attitude control and antenna steering required.

Scenario	**Max** C/N_0 **[dB-Hz]**	**Min** C/N_0 **[dB-Hz]**	**Peak-to-peak [dB]**	**Complexity**
1: Mutual pointing	52.48	40.45	12.03	High
2: Fixed Earth-pointing	17.26	−10.59	27.85	Low
3: Fixed TX, RX tracking	52.2	19.58	32.62	Medium

Table 4.1: Comparison of performance metrics and operational complexity for the three simulated scenarios.

From a performance standpoint, Scenario 4.1.1 clearly delivers the best results. Both antennas operate at maximum gain throughout the mission, leading to the highest C/N_0 levels and the smallest temporal variability. However, this configuration demands active, continuous tracking at both ends of the link, implying higher system complexity and control requirements.

Scenario 4.1.2 represents a much simpler geometry on the transmitter side, as the beacon remains oriented toward Earth. The spacecraft must still maintain its Earth-pointing attitude during its trajectory, but no dedicated tracking of the beacon is performed. This greatly simplifies operations but results in the lowest and most variable C/N_0 values due to frequent misalignments with the line-of-sight. Although short periods of improved performance occur, when the beacon–spacecraft distance reaches its minimum, these brief gains are not enough to counterbalance the overall geometric penalties.

Scenario 4.1.3 occupies an intermediate position. By keeping the beacon fixed toward Earth while allowing the receiver to actively track the beacon, it avoids the severe geometric losses of Scenario 4.1.2 and achieves C/N_0 values much closer to the ideal case, with peaks around 50 dB-Hz. Nevertheless, the fixed transmitter beam still causes significant variations (up to 30 dB peak-to-peak), especially when the spacecraft lies outside the beacon's main lobe.

Overall, the comparison highlights a fundamental trade-off: maximum performance is obtained when both ends actively track (Scenario 4.1.1) at the price of the highest operational complexity, Scenario 4.1.2 minimizes the complexity on the transmitter side but suffers from large geometric fluctuations, Scenario 3 instead

provides a balanced compromise, improving robustness without requiring active tracking on both sides. The choice between these architectures in future missions will therefore depend on the relative priorities assigned to link robustness, system complexity and resource constraints.

From the inverse link budget perspective, the most restrictive maximum transmit power across all scenarios is the 31.06 dBW obtained in Scenario 1. Scenarios 2 and 3, both using a fixed Earth-pointing beacon, resulted in the same worst-case value of 32.51 dBW, as they share identical geometric conditions toward Earth. Although the numerical difference is modest (about 1.5 dB), it is operationally relevant when defining beacon transmission policies that must respect the GPS L1 interference protection threshold. Since 31.06 dBW represents the most restrictive $P_{\mathrm{tx,max}}$ value observed among all scenarios, setting the beacon transmit power below this threshold ensures that the GPS L1 interference protection limit is never exceeded in any configuration. The nominal transmit power adopted in this study (16 dBW) is therefore safely within the allowed margin.

4.3 Performance Analysis of GNSS and Beacon Integration

This section provides an overall assessment of the navigation performance achieved along the simulated cislunar trajectory. The analysis focuses on a set of key indicators that describe both the radiometric and geometric quality of the GNSS-based solution, including the C/N_0, signal visibility and availability, DOP and the corresponding predicted position uncertainty derived from the assumed User Equivalent Range Error (UERE). All metrics are evaluated for each constellation and frequency band and then extended to include the contribution of the lunar beacon.

The C/N_0 was analyzed to characterize the radiometric conditions experienced by the receiver along the trajectory. For each satellite (identified by its PRN), all available C/N_0 samples were extracted over time and grouped by constellation. Although the simulator models multiple frequency bands for each GNSS system, in this analysis only the first operational band listed in Tables 3.1 and 3.3 was considered for each constellation. This choice was made because, for all systems, the distribution of C/N_0 values across different bands followed a very similar trend, so splitting the analysis by frequency would not provide additional insight.

For each constellation, all valid C/N_0 samples obtained on the selected band were concatenated into a single dataset representative of that system. Histograms were then generated to describe the overall time distribution of the received signal strength. The horizontal axis represents the cumulative duration during which a certain C/N_0 level is observed (expressed in hours), while the vertical axis

corresponds to the C/N_0 value in dB-Hz. Each horizontal bar therefore indicates how long the receiver spent in a given C/N_0 interval.

In addition to the per-constellation histograms, a global distribution was generated by combining the representative C/N_0 values from all constellations into a single dataset. This provides a compact view of the overall radiometric conditions along the trajectory and highlights the most frequently observed power ranges across the entire GNSS infrastructure.

The resulting histograms are reported in Figures 4.11 and 4.12.

As expected, most of the received signals fall within the low-power region, typically between 10 dB-Hz and 20 dB-Hz. This reflects the significant propagation losses at cislunar distances and the conservative antenna pointing adopted at both the transmitting and receiving sides. Signal levels above 30 dB-Hz occur only occasionally, in correspondence with particularly favourable geometric conditions in which the relative antenna orientation yields higher effective gain.

Differences among constellations mainly depend on the number of visible satellites and on the orbital configuration of each system. Global constellations such as GPS and Galileo exhibit broader and denser distributions, indicating longer cumulative observation times and a wider range of received power levels, as clearly visible in Figures 4.11a and 4.11b. Regional systems such as QZSS and IRNSS show shorter distributions, limited to specific time windows when their coverage overlaps with the spacecraft's line of sight.

The overall histogram confirms that the receiver spends the majority of the simulated period under weak signal conditions, with most samples below 20 dB-Hz (Figure 4.12). These results provide a comprehensive overview of the expected signal strength distribution in cislunar space and serve as a reference for subsequent analysis of visibility and navigation geometry.

The visibility analysis aims to quantify, at each epoch, the number of satellites that can be effectively used by the receiver. A satellite is considered visible only when two conditions are simultaneously met: a valid line-of-sight between the satellite and the receiver and a received C/N_0 above the sensitivity threshold of the tracking unit.

The geometric visibility is verified by checking whether the straight line connecting the spacecraft and the satellite intersects the spherical bodies representing the Earth or the Moon. If the line-of-sight is obstructed by either of them, the satellite is marked as geometrically hidden and is excluded from further consideration.

In addition to the geometric constraint, the received C/N_0 is computed for each frequency band based on the link-budget parameters. A satellite is classified as trackable only when the corresponding C/N_0 exceeds the predefined threshold, which represents the minimum signal level required by the receiver to maintain lock. For the analysis presented in this work, this threshold was set to 24 dB-Hz.

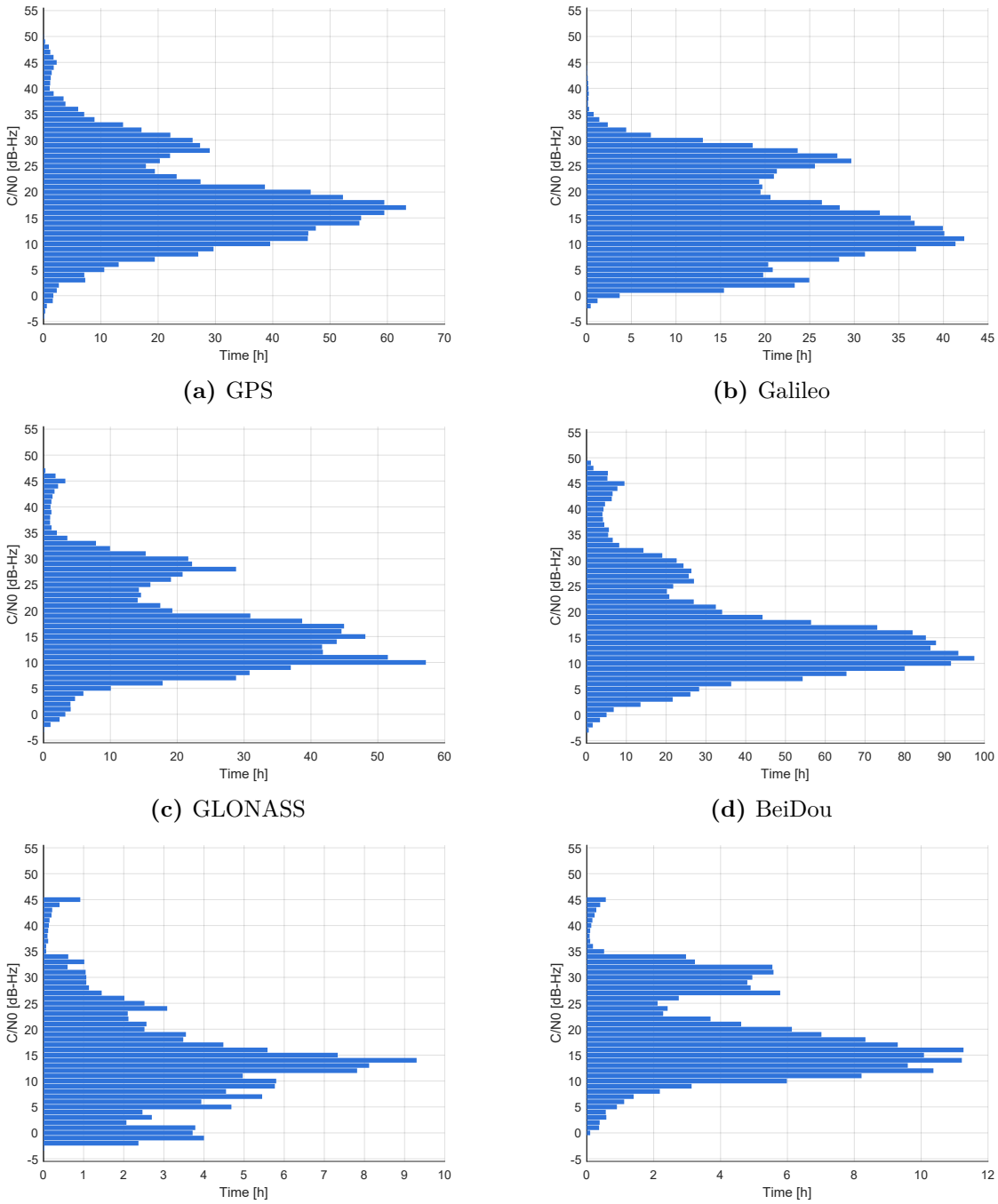

(a) GPS **(b)** Galileo

(c) GLONASS **(d)** BeiDou

(e) QZSS **(f)** IRNSS

Figure 4.11: Distribution of the received C/N_0 values for each GNSS constellation.

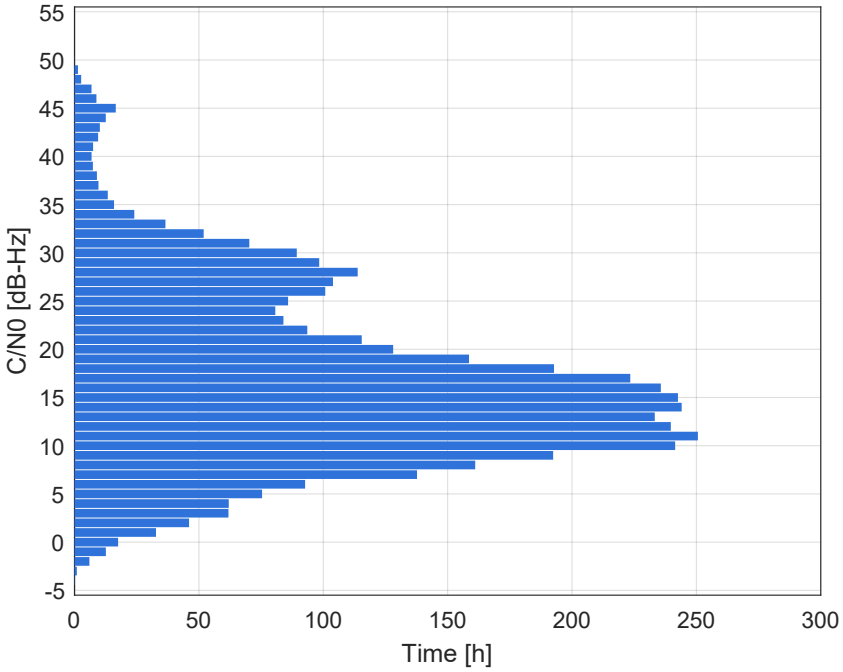

Figure 4.12: Overall C/N_0 histogram combining all constellations.

The resulting visibility therefore reflects both geometric and radiometric constraints, providing a realistic estimate of the number of satellites that could be tracked at each epoch. For every constellation and for each operational frequency band, the simulator records the number of visible satellites as a function of time, producing coverage time histories along the Earth-Moon transfer. The visibility curves are compared with the instantaneous receiver–Earth distance, highlighting the direct relationship between increasing range, signal attenuation and the progressive reduction in the number of observable satellites (Fig.4.13)

The visibility results show clear differences among the constellations and the frequency bands considered. Despite minor variations between bands, the general behaviour remains consistent, confirming that the impact of frequency on overall visibility is limited compared to geometric and power-related factors.

GPS and Galileo maintain the highest and most continuous visibility, with multiple satellites remaining above the tracking threshold for a significant portion of the simulated period. Their global coverage ensures stable performance even as the spacecraft moves away from Earth. BeiDou exhibits similar levels of visibility, though with stronger fluctuations caused by its mixed orbital geometry.

GLONASS presents a more irregular pattern, with interruptions reflecting less favorable satellite distribution at certain epochs. In contrast, QZSS and IRNSS are visible only intermittently, as expected for regional systems whose footprints

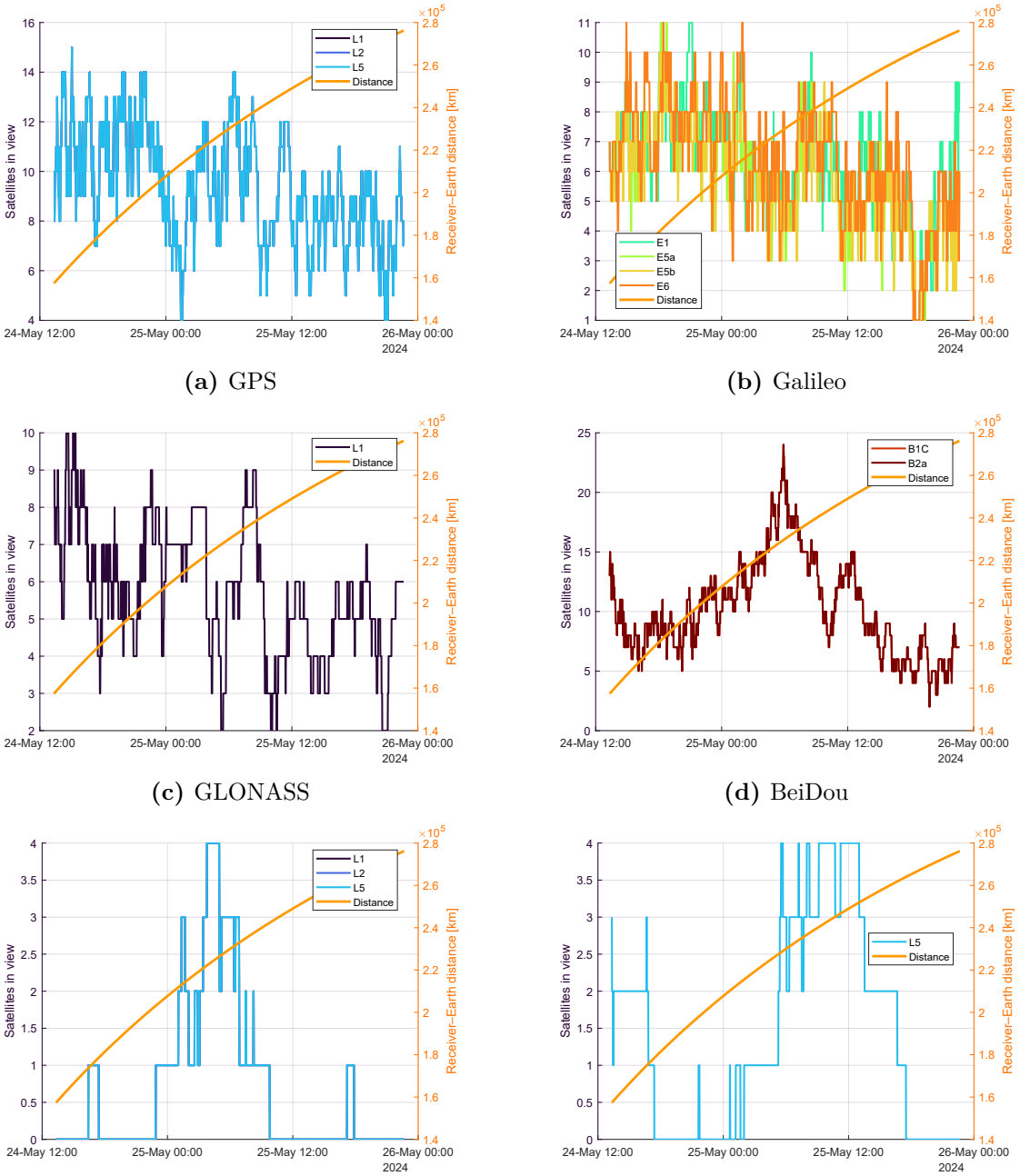

(a) GPS **(b)** Galileo

(c) GLONASS **(d)** BeiDou

(e) QZSS **(f)** IRNSS

Figure 4.13: Number of visible satellites for each GNSS constellation along the simulated trajectory (threshold = 24 dB-Hz).

intersect the trajectory only over limited intervals.

The gradual reduction in the number of observable satellites over time is mainly

driven by the increasing Earth–spacecraft distance. As the range grows, the free-space path loss intensifies, leading to lower received power and consequently reduced C/N_0 values. This radiometric attenuation, combined with less favourable geometry, explains the overall degradation of visibility in the later stages of the trajectory.

The availability analysis quantifies the fraction of epochs along the trajectory in which the receiver can determine a valid position solution. In this case, availability corresponds to the percentage of epochs where at least four satellites are simultaneously usable, meaning that they satisfy both geometric visibility and radiometric detectability conditions.

The Single Point Positioning (SPP) availability results, presented in Figure 4.14, show that all global constellations provide consistently high coverage along the simulated trajectory. GPS, Galileo, GLONASS and BeiDou maintain nearly full availability across all their operational frequency bands, confirming that a sufficient number of satellites remains visible and above the tracking threshold during most of the propagation. The limited differences observed between bands reflect variations in the frequency value and antenna patterns. As expected, the regional constellations QZSS and IRNSS exhibit much lower availability.

The total availability plot, comparing GNSS-only and GNSS+Beacon cases, shows that the inclusion of the lunar beacon does not significantly alter the overall percentage of epochs with sufficient satellites for positioning. This outcome is consistent with the beacon availability timeline, which indicates that the beacon is accessible only intermittently (Fig. 4.15). Since GNSS coverage alone already provides four or more usable signals during most of the trajectory, adding the beacon only marginally affects whether the minimum satellite count is reached. Its contribution is most relevant during the few short intervals in which the number of trackable GNSS satellites falls below four.

The limited impact of the beacon on availability should not be interpreted as a lack of usefulness. While it does not substantially increase the number of epochs with a valid position fix, its contribution is more pronounced in terms of geometry quality, as reflected by the improvement in Geometric Dilution of Precision (GDOP) when the beacon is active. In other words, the beacon acts less as a backup source that restores lost availability and more as a geometric enhancer that strengthens the positioning configuration whenever it is visible and above the signal threshold.

The accuracy of the position solution does not depend only on the number of satellites in view, but also on how they are distributed in space with respect to the receiver. Even with several usable links, a poor geometric configuration can lead to large position errors. This effect is quantified through the GDOP, a dimensionless indicator that expresses how the geometry of the transmitters amplifies measurement errors into uncertainty on the estimated position and clock offset. A low GDOP corresponds to a well-distributed configuration, where range

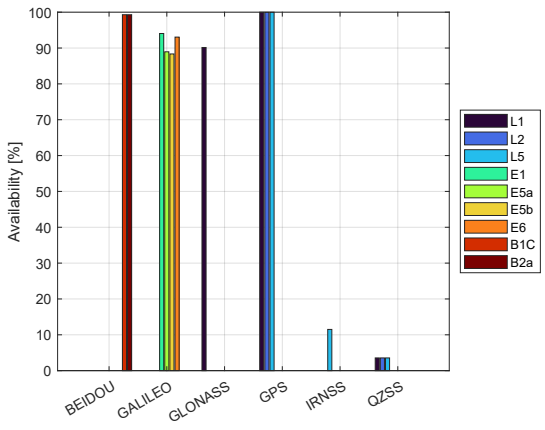

(a) SPP availability by constellation and band.

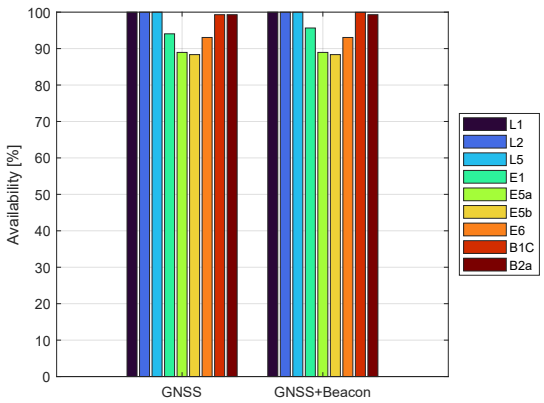

(b) Totals comparing GNSS-only and GNSS+Beacon.

Figure 4.14: Availability summary across systems and totals.

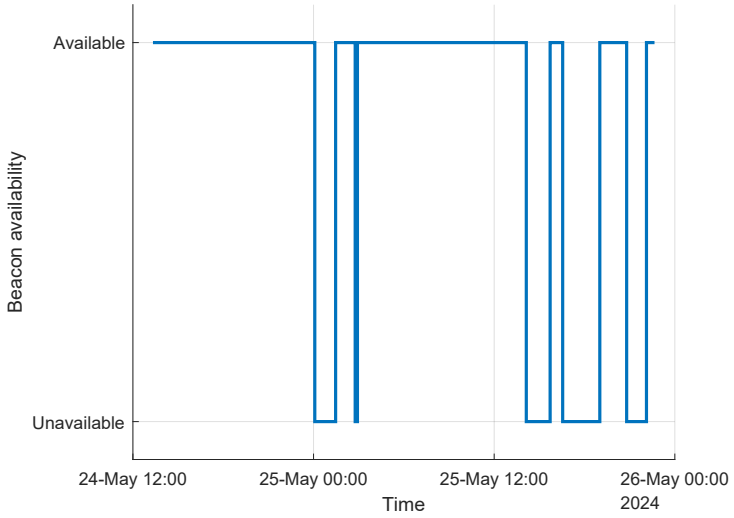

Figure 4.15: Beacon availability.

errors minimally affect the solution, while high GDOP values indicate poor geometry and degraded accuracy.

Before discussing the evolution of the geometry along the trajectory, it is useful to recall how the GDOP relates to the expected position-domain uncertainty. Assuming that all pseudorange measurements are affected by independent errors with identical standard deviation σ_{UERE}, the corresponding position error standard deviation can be approximated as

$$\sigma_{\mathrm{pos}} = \mathrm{GDOP} \times \sigma_{\mathrm{UERE}}. \tag{4.6}$$

so that GDOP directly acts as an amplification factor on the measurement noise.

At each epoch, once the set of usable links has been identified, those that satisfy both geometric visibility and signal strength conditions, the receiver position $\mathbf{r}$ and the transmitters' positions $\mathbf{s}_i$ are used to construct the geometry matrix $\mathbf{H}$. This matrix corresponds to the Jacobian of the pseudorange measurement model. For a single pseudorange

$$\rho_i = \|\mathbf{s}_i - \mathbf{r}\| + b, \tag{4.7}$$

the gradient with respect to the receiver state vector $[x,\, y,\, z,\, b]$ is

$$\frac{\partial \rho_i}{\partial \mathbf{x}} = \left[\frac{x - s_{ix}}{\|\mathbf{s}_i - \mathbf{r}\|},\ \frac{y - s_{iy}}{\|\mathbf{s}_i - \mathbf{r}\|},\ \frac{z - s_{iz}}{\|\mathbf{s}_i - \mathbf{r}\|},\ 1 \right]. \tag{4.8}$$

Introducing the compact notation for the corresponding line-of-sight unit vector,

$$\mathbf{u}_i = \frac{\mathbf{s}_i - \mathbf{r}}{\|\mathbf{s}_i - \mathbf{r}\|} = [\, u_{ix},\, u_{iy},\, u_{iz} \,]^\top, \tag{4.9}$$

the i-th row of the geometry matrix becomes

$$\mathbf{H}_i = [\, u_{ix},\, u_{iy},\, u_{iz},\, 1 \,], \tag{4.10}$$

which represents the gradient of the pseudorange measurement with respect to the state variables.

Stacking all N usable links yields

$$\mathbf{H} = \begin{bmatrix} u_{1x} & u_{1y} & u_{1z} & 1 \\ u_{2x} & u_{2y} & u_{2z} & 1 \\ \vdots & \vdots & \vdots & \vdots \\ u_{Nx} & u_{Ny} & u_{Nz} & 1 \end{bmatrix}, \tag{4.11}$$

which relates pseudorange residuals $\Delta\boldsymbol{\rho}$ to corrections in the estimated receiver position and clock bias $\Delta\mathbf{x} = [\, \Delta x,\, \Delta y,\, \Delta z,\, -\Delta b \,]^\top$ through the linearized model

$$\Delta\boldsymbol{\rho} = \mathbf{H}\, \Delta\mathbf{x} + \boldsymbol{\varepsilon}, \tag{4.12}$$

where $\boldsymbol{\varepsilon}$ includes measurement noise and residual modelling effects.

Assuming uncorrelated errors of equal variance σ^2, the covariance of the estimated parameters is proportional to the inverse of the normal matrix, $\mathbf{Q} = (\mathbf{H}^\top \mathbf{H})^{-1}$, and the GDOP is defined as

$$\mathrm{GDOP} = \sqrt{\mathrm{trace}(\mathbf{Q})} = \sqrt{\mathrm{trace}\Big((\mathbf{H}^\top \mathbf{H})^{-1}\Big)}. \tag{4.13}$$

This scalar value expresses how geometry alone affects the propagation of range errors into position and clock uncertainty. A meaningful GDOP can be computed only when at least four links are available, as this is the minimum required to estimate the four unknowns. Whenever the lunar beacon is available, it is treated as an additional transmitter and its line-of-sight vector contributes an extra row to the geometry matrix. The result is typically a more favourable configuration and a reduction in GDOP, reflecting the improved conditioning of the system.

The combined GDOP, obtained by merging all GNSS constellations, is shown in Figure 4.16a. At the beginning of the simulated period, when the spacecraft remains relatively close to Earth and visibility is high, the geometry is well conditioned and GDOP values stay low, typically between 8 and 20. As the distance from Earth increases, the visible portion of each constellation shrinks and becomes progressively less favourable, leading to higher GDOP values and more frequent fluctuations. The effect of including the lunar beacon is clearly visible in the same plot, where the red curve represents the GNSS+Beacon configuration: in the GNSS-only case, GDOP typically ranges between 50 and 300, with occasional peaks exceeding 600 during phases of poor geometry, whereas when the beacon is available GDOP remains between 5 and 15 for most of the trajectory, with only brief intervals around 30. This corresponds to an improvement of more than an order of magnitude over large portions of the arc. During periods when the beacon is not available, the two curves coincide, as confirmed by the correspondence with the beacon availability timeline in Figure 4.15.

The per-constellation behaviour reported in Figure 4.16c highlights the differences among systems, primarily driven by coverage and orbital distribution. The regional constellations, QZSS and IRNSS, display large fluctuations and recurrent spikes as a direct consequence of limited spatial coverage and the small number of satellites occasionally visible from the spacecraft. In contrast, the global constellations (GPS, Galileo, BeiDou, GLONASS) yield lower and more stable values, consistent with broader and more uniform geometries. Sharp peaks across all systems correspond to epochs where the number of usable satellites approaches the minimum requirement, making the geometry matrix nearly singular and amplifying the dilution effect.

To translate the geometric results into more practical terms, the GDOP values were later converted into an equivalent position error standard deviation using the relation in Eq. 4.6. The parameter σ_{UERE} accounts for the different contributions affecting each range measurement, such as receiver thermal noise, residual satellite clock and orbit errors, and hardware effects. For this analysis it was set to 10 m, a representative value for the expected conditions in the cislunar environment, where instrumental and modelling errors remain significant.

The resulting time history of the position error standard deviation is shown in Figure 4.17, comparing the GNSS-only and GNSS+Beacon configurations. The

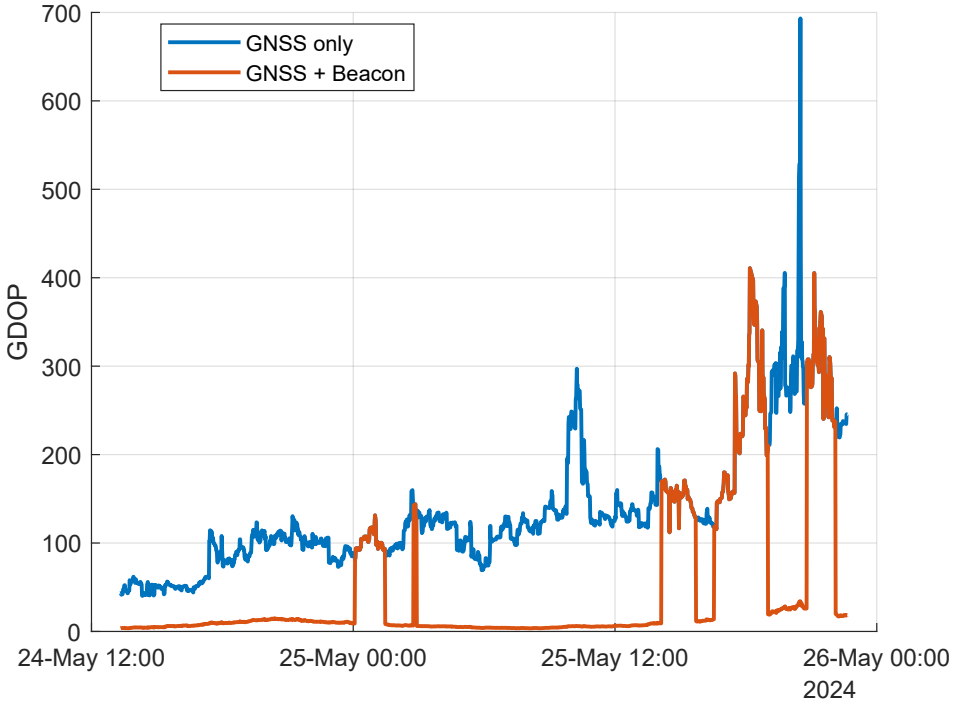

(a) Overall GDOP comparison between GNSS-only and GNSS+Beacon.

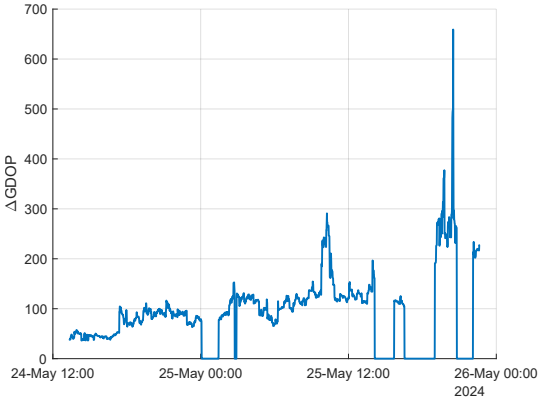

(b) GDOP delta.

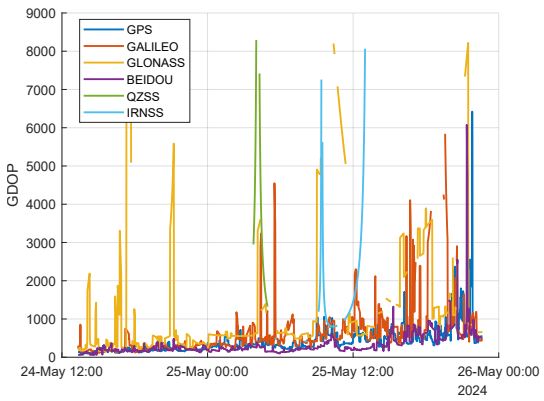

(c) GDOP evolution per individual constellation.

Figure 4.16: GDOP results along the trajectory.

GNSS-only curve generally ranges between about 0.5 km and 3 km for most of the trajectory, with several peaks exceeding 6 km during the periods of poorest geometry. When the lunar beacon is included, the standard deviation drops dramatically—remaining between roughly 50 m and 150 m for most of the time, and only rarely rising to a few hundred meters near the end of the simulated arc.

The two curves coincide whenever the beacon signal is not available, as already observed also in the GDOP plot (Figure 4.16a).

These values provide a clear, quantitative measure of the benefit introduced by the beacon. Even a single additional source located on the lunar surface leads to a reduction in the expected positioning uncertainty by more than one order of magnitude for large portions of the trajectory. This demonstrates the potential of lunar beacons to act as powerful geometric anchors, effectively complementing GNSS coverage and ensuring a more stable and accurate navigation capability in cislunar space.

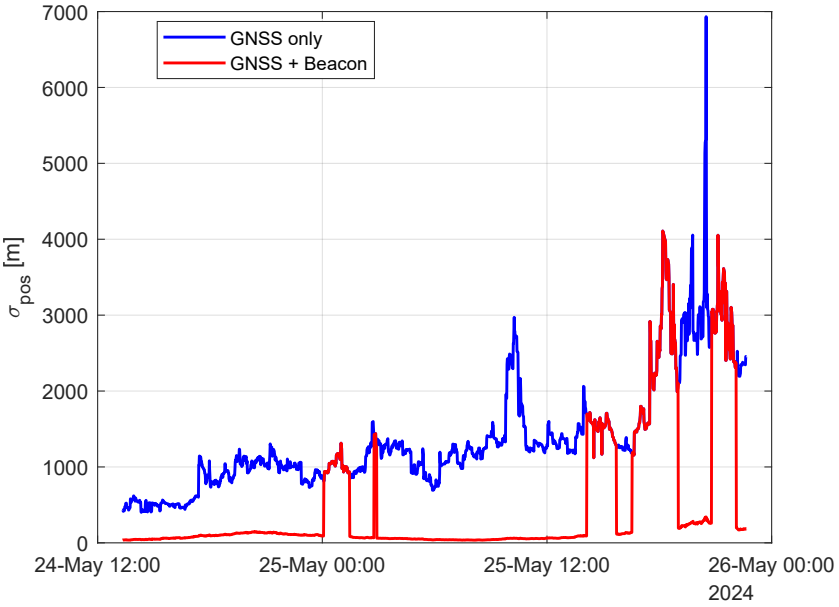

Figure 4.17: Positioning error standard deviation ($\sigma_{\mathrm{UERE}} = 10$ m).

Chapter 5

Conclusions

This work investigated the feasibility of extending GNSS-based navigation into the cislunar region and examined how the integrated of a single lunar beacon could enhance the overall navigation performance. The simulation framework developed for this study enabled a realistic evaluation of satellite visibility, signal strength and geometric configuration along a representative Earth–Moon transfer trajectory.

The results demonstrated that, although current global GNSS constellations were designed primarily for terrestrial and near-Earth applications, they can still provide meaningful support well beyond Earth orbit. When signals from multiple systems are combined, sufficient satellite visibility is maintained for a large portion of the trajectory, allowing continuous positioning even at considerable distances from Earth. However, as the spacecraft travels away from Earth, the geometry progressively degrades and the received power weakens, limiting the achievable accuracy.

The introduction of a single lunar beacon proved to be highly effective in mitigating this degradation. Whenever its signal was available, the beacon significantly improved the overall geometry, reducing GDOP by more than one order of magnitude and considerably enhancing the expected positioning accuracy. These results are particularly meaningful considering the simplicity of the configuration and the moderate transmission power assumed.

These improvements are particularly interesting considering the simplicity of the configuration and the relatively modest transmission power assumed in the analysis. At the same time, the benefit is not uniform along the entire arc and depends on the relative position between the spacecraft and the surface transmitter, which means that a single beacon cannot address all limitations inherent to deep-space navigation. Rather than replacing the need for future dedicated lunar navigation systems, the results suggest that even a minimal aiding element can provide a useful intermediate step, especially during early missions or for scenarios where resources are limited. A beacon of this kind could complement existing GNSS

signals and help improve robustness without requiring the deployment of a full constellation from the outset.

Overall, this study shows that the combination of global GNSS signals with even a single lunar aiding source represents a realistic and efficient step toward future lunar navigation architectures. Such an approach can ensure robust, autonomous and continuous positioning for upcoming missions, supporting the broader goal of establishing a sustained human presence in the lunar environment.

Bibliography

[1] L. Iess, M. Di Benedetto, N. James, M. Mercolino, L. Simone, and P. Tortora. «ASTRA: Interdisciplinary study on enhancement of the end-to-end accuracy for spacecraft tracking techniques». In: *Acta Astronautica* 94.2 (2014), pp. 699–707 (cit. on p. 1).

[2] E. Turan, S. Speretta, and E. Gill. «Autonomous navigation for deep space small satellites: Scientific and technological advances». In: *Acta Astronautica* 193 (2022), pp. 56–74 (cit. on pp. 1, 3).

[3] NASA. *Artemis Program Overview*. Official NASA website. 2020. URL: `https://www.nasa.gov/humans-in-space/artemis/` (cit. on p. 1).

[4] European Space Agency. *Moonlight: bringing connectivity and navigation to the Moon*. Official ESA website. 2021. URL: `https://www.esa.int/Applications/Connectivity_and_Secure_Communications/Moonlight` (cit. on p. 1).

[5] A. Delepaut, P. Giordano, J. Ventura-Traveset, D. Blonski, M. Schönfeldt, P. Schoonejans, S. Aziz, and R. Walker. «Use of GNSS for lunar missions and plans for lunar in-orbit development». In: *Advances in Space Research* 66.12 (2020), pp. 2739–2756 (cit. on pp. 1, 10).

[6] NASA. *NASA Successfully Acquires GPS Signals on Moon*. Official NASA news release, about LuGRE results. 2025. URL: `https://www.nasa.gov/directorates/somd/space-communications-navigation-program/nasa-successfully-acquires-gps-signals-on-moon/` (cit. on p. 1).

[7] Oliver Montenbruck, M. Markgraf, M. Garcia-Fernandez, and A. Helm. «GPS for Microsatellites – Status and Perspectives». In: *Small Satellites for Earth Observation*. Springer, 2008, pp. 165–174 (cit. on pp. 3, 10).

[8] A.-Z. Amir, A. El-Mowafy, et al. «Precise Orbit Determination of LEO Satellites Based on Undifferenced GNSS Observations». In: *Journal of Surveying Engineering* 147.1 (2021) (cit. on p. 3).

[9] J. L. Burch, T. E. Moore, R. B. Torbert, and B. L. Giles. «Magnetospheric Multiscale Overview and Science Objectives». In: *Space Science Reviews* 199.1 (2016), pp. 5–21. DOI: 10.1007/s11214-015-0164-9 (cit. on p. 3).

[10] Joel J. K. Parker, Frank H. Bauer, Benjamin W. Ashman, James J. Miller, Werner Enderle, and Daniel Blonski. «Development of an Interoperable GNSS Space Service Volume». In: *Proceedings of the 31st International Technical Meeting of the Satellite Division of The Institute of Navigation (ION GNSS+ 2018)*. 2018, pp. 1246–1256 (cit. on p. 4).

[11] Almat Raskaliyev, Sarosh Hosi Patel, Tarek M. Sobh, and Aidos Ibrayev. «GNSS-Based Attitude Determination Techniques—A Comprehensive Literature Survey». In: *IEEE Access* 11 (2023) (cit. on p. 4).

[12] MIT Haystack Observatory. *Using GNSS to Measure Ionospheric TEC*. Online. 2018. URL: https://www.haystack.mit.edu (cit. on p. 4).

[13] Naifeng Fu and Fenghui Li. «An Introduction of GNSS Reflectometer Remote Sensing Mission From Yunyao Aerospace Technology Co., Ltd.» In: *Proceedings of the IEEE*. 2021 (cit. on p. 4).

[14] Oliviero Vouch, Andrea Nardin, Alex Minetto, Matteo Valvano, Simone Zocca, and Fabio Dovis. «A Customized EKF model for GNSS-based Navigation in the Harsh Space Environment». In: *2023 IEEE International Conference on Wireless for Space and Extreme Environments (WiSEE)*. 2023, pp. 13–18. DOI: 10.1109/WiSEE58383.2023.10289208 (cit. on pp. 5, 13, 16).

[15] Andrea Nardin, Alex Minetto, Oliviero Vouch, Margherita Mariani, and Fabio Dovis. «Snapshot Acquisition of GNSS Signals in Space: a Case Study at Lunar Distances». In: *Proceedings of the 35th International Technical Meeting of the Satellite Division of The Institute of Navigation (ION GNSS+ 2022)*. 2022, pp. 3603–3617. DOI: 10.33012/2022.18477 (cit. on pp. 5, 6).

[16] Frank H. Bauer, Michael C. Moreau, Frederic Dahle-Melsaether, and E. Glenn Lightsey. «Results from the GPS Experiment on Equator-S». In: *Proceedings of the Institute of Navigation GNSS Conference* (1999). First demonstration of GPS side-lobe signal tracking beyond MEO. URL: https://www.researchgate.net/publication/224781913_Results_from_the_GPS_Experiment_on_Equator-S (cit. on p. 10).

[17] United Nations Office for Outer Space Affairs. *The Interoperable Global Navigation Satellite Systems Space Service Volume*. Tech. rep. Official ICG/UNOOSA publication defining GNSS performance beyond MEO. Vienna: UNOOSA, 2018. URL: https://www.unoosa.org/res/oosadoc/data/documents/2018/stspace/stspace75_0_html/st_space_75E.pdf (cit. on p. 10).

[18] Benjamin W. Ashman, Joel J. K. Parker, Frank H. Bauer, and Michael Esswein. *Exploring the Limits of High Altitude GPS for Future Lunar Missions*. Tech. rep. AAS 18-082, NASA technical report exploring GPS performance for lunar missions. NASA Goddard Space Flight Center, 2018. URL: https://ntrs.nasa.gov/api/citations/20180001247/downloads/20180001247.pdf (cit. on p. 10).

[19] Luke B. Winternitz, Anne C. Long, M. Haroon Chaudhry, A. Konitzer, et al. «The Lunar GNSS Receiver Experiment (LuGRE)». In: *Proceedings of the 2022 International Technical Meeting of The Institute of Navigation (ION ITM)*. NASA/ASI experiment concept and performance prediction for GNSS reception in lunar orbit. Long Beach, CA, 2022. URL: https://ntrs.nasa.gov/api/citations/20220002074/downloads/LuGRE_ION-ITM_2022_Draft8_Submitted_ConferenceProceedings.pdf (cit. on p. 11).

[20] Joel Parker et al. *Lunar GNSS Receiver Experiment (LuGRE) Mission Data*. Version v1. Zenodo, Oct. 2025. URL: https://zenodo.org/records/16411687 (cit. on p. 11).

[21] NASA Space Communications and Navigation (SCaN) Program. *LunaNet Interoperability Specification (Version 5) Baseline*. Tech. rep. Defines the technical framework and standards for interoperable lunar communication and navigation services. NASA Goddard Space Flight Center, 2025. URL: https://www.nasa.gov/wp-content/uploads/2025/02/lunanet-interoperability-specification-v5-baseline.pdf (cit. on pp. 11, 12).

[22] Katherine Schauer, Danny Baird, and Dave Israel. *LunaNet: Empowering Artemis with Communications and Navigation Interoperability*. NASA article describing the LunaNet architecture and services. Oct. 2021. URL: https://www.nasa.gov/general/lunanet-empowering-artemis-with-communications-and-navigation-interoperability/ (cit. on p. 11).

[23] European Space Agency. *ESA's Moonlight Programme: Pioneering the Path for Lunar Exploration*. ESA official article on the Moonlight LCNS programme. Oct. 2024. URL: https://www.esa.int/Applications/Connectivity_and_Secure_Communications/ESA_s_Moonlight_programme_Pioneering_the_path_for_lunar_exploration (cit. on p. 12).

[24] Lihua Zhang. «Development and Prospect of Chinese Lunar Relay Communication Satellite». In: *Journal of Deep Space Exploration* 8.2 (2021), pp. 95–110. DOI: 10.34133/2021/5573843 (cit. on p. 12).

[25] Chunlai Li, Zuo Wei, Weibin Wen, and et al. «Overview of the Chang'e-4 Mission: Opening the Frontier of Scientific Exploration of the Lunar Far Side». In: *Space Science Reviews* 217.2 (2021), pp. 1–28. DOI: 10.1007/s11214-021-00793-z (cit. on p. 12).

[26] The Planetary Society. *Queqiao-2: China's bridge for lunar exploration*. Accessed: Nov. 25, 2025. Mar. 2024. URL: https://www.planetary.org/space-missions/queqiao-2-chinas-bridge-for-lunar-exploration (cit. on p. 12).

[27] Jeff Foust. «Lockheed Martin subsidiary to offer commercial lunar communications and navigation services». In: *SpaceNews* (Mar. 2023) (cit. on p. 13).

[28] Oliviero Vouch, Andrea Nardin, Alex Minetto, Simone Zocca, Matteo Valvano, and Fabio Dovis. «Aided Kalman Filter Models for GNSS-Based Space Navigation». In: *IEEE Journal of Radio Frequency Identification* 8 (2024), pp. 535–546 (cit. on p. 13).

[29] Joel J. K. Parker, Frank H. Bauer, Benjamin W. Ashman, James J. Miller, Daniel Blonski, Benjamin W. Anderson, and et al. *The Lunar GNSS Receiver Experiment (LuGRE)*. Tech. rep. 20220002074. NASA Goddard Space Flight Center, 2022. URL: https://ntrs.nasa.gov/citations/20220002074 (cit. on p. 15).

[30] Jennifer E. Donaldson, Jason J. K. Parker, Michael C. Moreau, D. Ena Highsmith, and Paul D. Martzen. «Characterization of On-Orbit GPS Transmit Antenna Patterns for Space Users». In: *NAVIGATION* 67.3 (2020), pp. 411–438. DOI: 10.1002/navi.377 (cit. on p. 19).

[31] Joint Research Centre (JRC). *Galileo Reference Antenna Pattern (GRAP) - Version 1.0*. Tech. rep. Available as internal documentation with attached pattern files. European Commission, 2021. URL: https://publications.jrc.ec.europa.eu/repository/handle/JRC124418 (cit. on p. 21).

[32] Oliver Montenbruck, Peter Steigenberger, Steffen Thölert, Daniel Arnold, and Georg Bury. «GNSS visibility and performance implications for the GENESIS mission». In: *Journal of Geodesy* 97.10 (2023), p. 96. DOI: 10.1007/s00190-023-01746-0 (cit. on p. 21).

[33] MathWorks. *gnssconstellation — Satellite Positions and Velocities*. Navigation Toolbox Documentation. 2024. URL: https://www.mathworks.com/help/nav/ref/gnssconstellation.html (visited on 10/17/2025) (cit. on p. 23).

[34] *QZSS Antenna Patterns*. Tech. rep. Publicly released gain pattern measurements for QZS-1R through QZS-7. Cabinet Office, Government of Japan, July 2023 (cit. on p. 24).

[35] Agenzia Spaziale Italiana. *LuGRE – Lunar GNSS Receiver Experiment*. https://www.asi.it/vita-nello-spazio/litalia-sulla-luna/lugre-lunar-gnss-receiver-experiment/ (cit. on p. 42).

[36] *IS-GPS-200N: Navstar GPS Space Segment / Navigation User Interfaces*. https://www.navcen.uscg.gov/sites/default/files/pdf/gps/IS-GPS-200N.pdf. Revision N, 01-AUG-2022. Aug. 2022 (cit. on pp. 47, 49).